COMPRESSIVE SENSING AND TIME REVERSAL BEAMFORMING APPROACHES FOR ULTRASOUND IMAGING

NOURA HANTIRA

A THESIS SUBMITTED TO THE FACULTY OF GRADUATE STUDIES
IN PARTIAL FULFILLMENT OF THE REQUIREMENTS FOR THE DEGREE OF
MASTERS OF APPLIED SCIENCE

GRADUATE PROGRAM IN ELECTRICAL ENGINEERING AND COMPUTER SCIENCE
YORK UNIVERSITY
TORONTO, ONTARIO

JULY 2015

ABSTRACT

The objective of this thesis is to develop a novel beamforming technique for ultrasound machines that enables field reconstruction at sampling rates much lower than the Nyquist rate. In our simulations, we use Field II, a MATLAB based program for simulating transducer fields and models of biological tissues for imaging applications. Field II is capable of generating the emitted and pulse-echo fields for a large number of transducers configurations, including linear, circular, and rectangular arrays. Once the ultrasound field is determined, the proposed imaging technique is applied to the received signals to reconstruct the image for reference biological tissues. Applying different adaptive beamforming techniques, including the delay and sum (DAS) and Capon algorithms, the received signals from Field II simulation program are used to render the ultrasound images. A second goal of the thesis is to apply compressive sensing (CS) on received signals to reconstruct full-length signals from a reduced number of samples. A third goal is to couple the principal of time reversal (TR) with compressive sensing to extend the CAPON beamformer for reconstructing images of biological tissues at low sampling frequencies in rich multipath environments. The outputs of compressive sensing and CAPON-based algorithms, alone or in conjunction with each other, are severely degraded in such environments. Through numerical simulations, I illustrate an enhancement in reconstructed quality of images depicting biological tissues with my time-reversal based compressive sensing, CAPON approach.

ACKNOWLEDGEMENTS

I would like to start by thanking my supervisor, Prof. Amir Asif, for his continuous support, professionally and financially. Despite his busy schedule, he was always there for me when I needed help. I want to also thank Prof. Mokhtar Aboelaze, who continuously provided guidance throughout my studies, as well as all my committee members for the effort they put in reviewing my thesis.

I want to thank my role model, my father who strongly believes in me, my two mothers who are always surrounding me with their love and care and my three siblings for their continuous support and encouraging words that guided me to where I am now. I can’t forget my father in-law whose words are still the big source of motivation for me. You may not be physically here, but I am sure you feel it. I would also like to thank my in-laws for being there when I needed.

At last, a special thanks goes to my loving husband who believes in me more than myself. I will never forget your help and support, Ihab. I wouldn’t have done it without you standing by my side. I want to also thank my two sons, Mostafa and Ahmed for their patience during my study years.

Table of Contents

Abstract ……………………………………………………………………………...ii

Acknowledgments……..………………………………………………………………iv

Table of Contents………………………………………………………………………v

List of Figures…………………………………………………………………………vii

Chapter 1 Introduction 1

Chapter 2 Introduction to Beamforming 7

2.1 Models Implemented Using Field II 8

2.1.1 Test Environment 9

2.2 Beamforming Algorithms 17

2.2.1 Delay and Sum Beamforming Algorithm 17

2.2.2 Capon Algorithm 19

2.3 Results of DAS Vs. CAPON algorithms 21

Chapter 3 Introduction to Compressive Sensing 25

3.1 What is Compressive Sensing? 26

3.2 Sensing Matrices 29

3.2.1 Binary Sensing Matrices 30

3.2.2 Bernoulli Sensing Matrices 31

3.3 Basis Matrices 33

3.4 Compressive Sensing Results 35

3.5 Summary 43

Chapter 4 Introduction to Time Reversal 46

4.1 What is Time Reversal 46

4.2 Time Reversal Implementation Using Field II 47

4.3 Time Reversal Results 51

Chapter 5 Time Reversal with Compressive Sensing 55

5.1 Results 57

5.2 Comparison between CS and TR with CS 57

Chapter 6 Conclusions 64

Bibliography 67

LIST OF FIGURES

Figure 1: Linear geometry of the transducer array used in the thesis. 9

Figure 2: Point scatter models implemented using Field II. 11

Figure 3: Cyst models implemented using Field II. 13

Figure 4: An example of the fetus phantom simulated using Field II. 15

Figure 5: An example of the kidney phantom simulated using Field II. 16

Figure 6: Block diagram illustrating the principal of the DAS beamformer. 18

Figure 7: Beamformed Images for the 2-point scatter using (a) DAS algorithm, (b) CAPON algorithm 22

Figure 8: Beamformed Images for the 10-point scatter using: (a) DAS algorithm, and (b) CAPON algorithm. 22

Figure 9: Beamformed Images for the 5-Cyst phantom using: (a) DAS algorithm, and (b) CAPON algorithm. 23

Figure 10: Beamformed Images for the 10-Cyst phantom using: (a) DAS algorithm, and (b) CAPON algorithm. 23

Figure 11: Schematic diagram representing compressive sampling. 26

Figure 12: Signal reconstructed using the binary sensing matrix versus the original signal 31

Figure 13: Signal reconstructed using the Bernoulli sensing matrix versus the original signal 33

Figure 14: Reconstruction using the DCT basis function. 34

Figure 15: Reconstruction using the WA basis function. 35

Figure 16: Implementation block diagram for compressive sensing. 37

Figure 17: Beamformed image reconstructed from decimated data for the 2-point scatter simulation: (a) Image using original diagonal data; (b) Decimation factor of 4; (c) Decimation factor of 6; (d) Decimation factor of 10. 39

Figure 18: Beamformed image reconstructed from decimated data for the 10-point scatter simulation: (a) image using original diagonal data; (b) Decimation factor of 4; (c) Decimation factor of 6; (d) Decimation factor of 10 40

Figure 19: Beamformed image reconstructed from decimated data for the 5-cyst phantom simulation: (a) image using original diagonal data; (b) Decimation factor of 4; (c) Decimation factor of 6; (d) Decimation factor of 10. 41

Figure 20: Beamformed image reconstructed from decimated data for the 5-cyst phantom simulation: (a) image using original diagonal data; (b) Decimation factor of 4; (c) Decimation factor of 6; (d) Decimation factor of 10. 42

Figure 21: Beamformed image reconstructed from decimated data for the fetus phantom simulation: (a) No decimation; (b) Decimation factor of 4; (c) Decimation factor of 6; (d) Decimation factor of 10 44

Figure 22: Beamformed image reconstructed from decimated data for the kidney phantom simulation: (a) No decimation; (b) Decimation factor of 4; (c) Decimation factor of 6; (d) Decimation factor of 10. 45

Figure 23: SIMO configuration: Step 1 of the TR mode of operation............................ 48

Figure 24: MIMO Configuration: Step of the TR mode of operation. 50

Figure 25: Schematic diagram illustrating how TR is used for beamforming ultrasound system. 50

Figure 26: Beamformed Images for the 5-Cyst phantom setup using the SIMO TR signals for (a) SNR = 20 dB; (b) SNR = 30 dB; (c) SNR = 40 dB. 52

Figure 27: Beamformed Images for the 5-Cyst phantom setup using the MIMO TR signals for (a) SNR = 20 dB; (b) SNR = 30 dB; (c) SNR = 40 dB. 53

Figure 28: Bar chart comparing SSIM values of MIMO and SIMO configurations for the 5 cyst phantom setup... 54

Figure 29: CS TR/BF mechanism that couples time reversal with compressive sensing.55

Figure 30: Beamformed Images for the 5-Cyst phantom using the CS TR/BF setup, for (a) the SIMO configuration; (b) the MIMO configuration. The decimation factor used in the CS setup is 4... 58

Figure 31: Beamformed Images for the 5-Cyst phantom using the CS TR/BF setup, for (a) the SIMO configuration, (b) the MIMO configuration. The decimation factor used in the CS setup is 6... 59

Figure 32: Beamformed Images for the 5-Cyst phantom using the CS TR/BF setup for: (a) the SIMO configuration; (b) the MIMO configuration. The decimation factor used in the CS setup is 10.. 60

Figure 33: Comparison between images obtained using reconstructed RF data with CS versus reconstructed RF data using CS TR processing for different decimation factors: (a) Decimation factor of 4; (b) Decimation factor of 6; (c) Decimation factor of 10...... 62

Chapter 1
Introduction

Ultrasound imaging uses high-frequency sound waves to view soft tissues such as body muscles and internal human organs. Because ultrasound images are captured in real-time, they can show snapshots of the body's internal organs in addition to be used for monitoring circulation of blood through arteries and veins within a human body.

In an ultrasound exam, a series of hand-held transducers are typically placed adjacent to the human body against the skin. Depending on the mode of operation, a subset of transducer elements send out high frequency sound waves that reflect off the body structures. The reflected sound waves, also referred to as backscatters or echoes, are recorded and processed using sophisticated signal processing algorithms to be displayed as an image that provides a fairly accurate representation of the internal human anatomy. Such ultrasound images are used by physicians in medical examinations. The signal processing algorithms use the frequency and strength (amplitude) of the backscatters, the time they take to return, and the change in the properties of the waveforms to generate the image of the internal organs. In signal processing, the process of forming images of the probed environment from backscattered signals is referred to as **Beamforming.**

Typically, an ultrasound transducer element works both as a transmitter (that generates sound waves) and a receiver (that observes sound waves). The ultrasound pulse is quite short in duration. Since it traverses in a straight path, it is often referred to as an ultrasound beam. The direction of ultrasound propagation along the beam is called the axial direction, and the direction in the image plane perpendicular to the axial direction is referred to as the lateral direction. Usually only a fraction of the transmitted pulse is reflected from the body tissues and returns as backscatters, while the remainder of the pulse continues to propagate along the axial direction to traverse greater tissue depths.

In this thesis, two different beamforming algorithms, namely, the Delay and Sum (DAS) algorithm and Capon algorithm, are implemented. Although the DAS beamforming algorithm is used in a variety of ultrasound machines, it does not the perceived image quality of the reconstructed images is poor, especially in complex environments, as is the case in imaging cysts or real body parts as compared to medium with point targets. I show reconstructed results of both algorithms to illustrate the superiority of the Capon algorithm over the DAS algorithm.

Another goal of this thesis is to apply compressive sensing (CS) on the raw radio frequency (RF) data received at each transducer element prior to the beamforming stage. Compressive sensing allows reconstruction of signal from a reduced number of samples, much lower than those obtained on the basis of the classical Nyquist rate. In the thesis, I investigate how well the CS algorithm works with different types of sensing matrices used to subsample the recorded data. Two types of sensing matrices tested in the thesis are the Binary matrix and Bernoulli matrix.

The third goal of the thesis is to apply the principal of time reversal (TR) to the CS, CAPON beamforming algorithm. On its own, the CS, CAPON algorithm is negatively impaired in environments with rich multipath. Coupling TR with the algorithm improves the quality of reconstruction of biological tissues. TR is applied for two different setups. The first setup is the Single Input Multiple Output (SIMO) configuration, where a single transducer element illuminates a section of the human body with the backscatters collected by the entire transducer array. The second setup is the Multiple Input Multiple Output (MIMO) configuration, where a larger number of transducer elements probes the human body. In my research, I show that images reconstructed using the MIMO configuration are of much better quality than images reconstructed using the SIMO configuration. Compressive sensing is applied in conjunction with TR to acquire data at a much reduced sampling rate. I compare the quality of the beamformed images obtained using compressive sensing alone (i.e., without TR) with images obtained by applying compressive sensing with TR. In both cases, the CAPON beamforming algorithm is applied to reconstruct the image of the reference body organ.

The simulation environment used to generate the backscatter observations is based on a customized MATLAB tool, Field II, which is a free software made available for educational research. I compare the beamformed images based on both perceived quality by including the actual images and quantitative measures, such as the structural similarity index (SSIM). The later criteria assesses the quality of the images based on the degradation of structural information in the reconstructed image as compared to the original image.

Organization of the thesis:

The thesis is organized as follows:

- Chapter 2 reviews two beamforming algorithms, namely the Delay-and-Sum (DAS) algorithm and the Capon algorithm. Field-II is introduced along with the five setups used to test the performance of the approaches presented in the thesis. The simulation setups used in the thesis include the 2-point and 10-point scatters field, 5-cyst and 10-cyst framework, the kidney phantom, and the fetus phantom within the human body. I also show the results of the beamforming algorithms using the entire dataset (without any compression) to provide the reference quality of reconstructed images used in the rest of the thesis.

- Chapter 3 introduces the concept of compressive sensing and how it is applied to the radio-frequency (RF) data. Different types of sensing matrix , including the Binary and Bernoulli matrices, are tested. Also, different types of basis matrices are tested showing the quality of the reconstructed data in each case. Beamformed images using data at different sampling rates are included for the setups implemented in Chapter 2.
- Chapter 4 explains the principle of time reversal and explains how it is implemented. Two configurations, namely SIMO and MIMO, are physically implemented using Field II. Beamformed images based on the time reversal observations are also presented in this chapter. I illustrate the improvement in the image quality obtained using time reversal over images reconstructed form the conventional data acquisition approach..
- Chapter 5 illustrates how time reversal and compressive sensing are coupled to effectivity reduce the sampling rate at which date is being acquired. SSIM compares beamformed images reconstructed using compressive sensing

coupled with time reversal versus images reconstructed using compressive sensing only.

- Chapter 6 concludes the thesis and presents directions for future work that can be considered an extension of this research.

Chapter 2
Introduction to Beamforming

As previously mentioned, a series of transducer elements can be configured as a linear transducer array to record the backscatters at several locations in close proximity to each other, which enables a more accurate and detailed representation of the human body. Likewise, during the transmitting stage, the probing signal can originate from a single transducer element in the Single Input Multiple Output (SIMO) configuration or from some combination of elements simultaneously in the multiple-input, multiple-output (MIMO) configuration.

Different beamforming algorithms have been proposed to reconstruct the beamformed image for localizing point targets or scatters within the human body. The point targets are of special interest to the physicians since they can potentially represent unnatural deformations or growths like cancer cells or tumours. In this thesis, we are implementing two beamforming (BF) algorithms, namely the delay-and-sum (DAS) and Capon [1] algorithms.

The input of any beamforming algorithm is the set of backscatters recorded by a linear array of transducer elements and the output is the reconstructed image of the section of the human body being examined. The region of interest includes anomalies in the human body behaving as acoustic scatters, which reflect the probing signal(s) transmitted to them due to the difference between the acoustic properties of the medium and scatters. The goal is to beamform the received signals and produce an image, which shows the locations of these scatters as accurately as possible in a two dimensional (2D) space.

2.1 Models Implemented Using Field II

In this thesis, the radio frequency (RF) data was simulated using Field II [2], a toolbox in MATLAB used for simulating ultrasound transducer fields and ultrasound models of biological tissues. Field II simulates the emitted and pulse-echo fields for both the pulsed and continuous form of waves for an array of transducers. Once the acoustic field is determined, an imaging technique such as the DAS or Capon is applied to the received signals in order to produce the image representing the modeled biological tissue.

Field II is capable of modeling different configurations of transducer arrays as well as different shapes, including linear, circular, and rectangular arrays. The program computes the ultrasounds field through the spatial impulse response. When the transducer is excited by a Dirac delta function, this response assigns the emitted ultrasound field at a specific point in space as a function of time. The probing signals for all kinds of excitation functions are calculated by convolving the spatial impulse response with the excitation function. The impulse response changes as a function of position relative to the transducer. The backscatters response in pulse-echo is calculated by convolving the transducer excitation function first with the spatial impulse response of the emitting aperture and a second time with the spatial impulse response of the receiving aperture. Finally, the electro-mechanical transfer function is also considered.

2.1.1 Test Environment

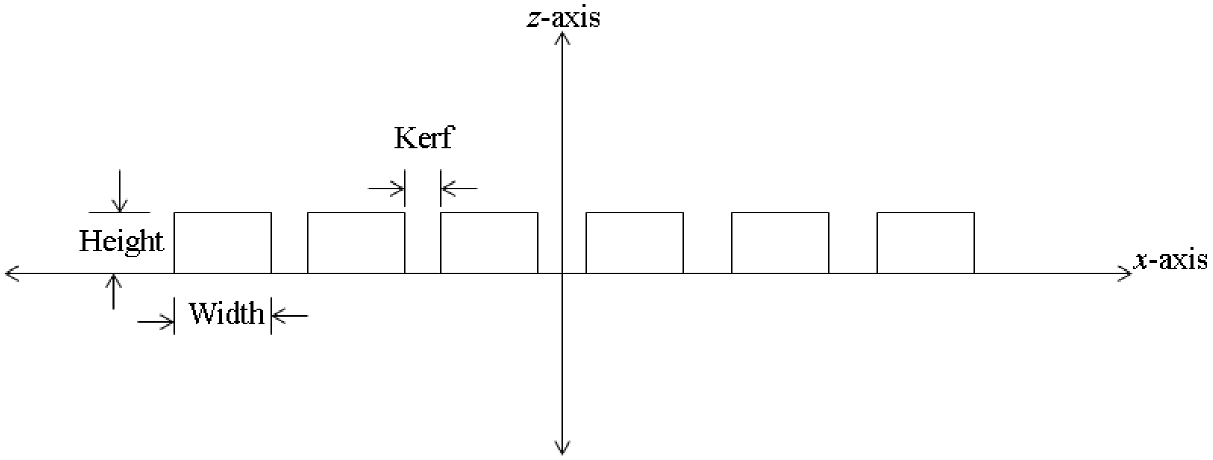

Figure 1: Linear geometry of the transducer array used in the thesis.

In all the experiments conducted in this thesis, a linear array of transducers as illustrated in Fig.1 is used. The array consists of 128 or 160 transducer elements arranged along the horizontal axis (*x*-axis) of the two dimensional (2D) domain.

For a 128-element array, the array starts from -31.1mm to 31.1mm along the *x*-axis with kerf (the distance between two consecutive transducer elements) equal to 0.5 mm. The width and height of each element is lambda λ and 5mm respectively, where λ is the wavelength and is equal to c/f_0, c is the propagation speed of sound in water and is equal to 1540 m/sec. Each transducer element emits a probing signal with a centre frequency (f_0) of 3.5MHz and a sampling frequency (f_s) of 100 MHz.

All experiments conducted in this thesis use a linear array of transducers. Using more complicated array configuration such as two or three dimensional, circular, or triangular configuration provides more accurate and robust observations. These, however, result in much more computationally intensive beamforming algorithms. Since the focus of the thesis is real-time implementation of the ultrasound machines at a much low cost, I restrict myself to the linear array configuration.

Using Field II, different models were implemented to simulate the region of interest. Fig. 2 shows the image truth for the 2-point target and 10-point target. Fig. 3 shows the image truth for a section of simulated setup with 5 cysts and 10

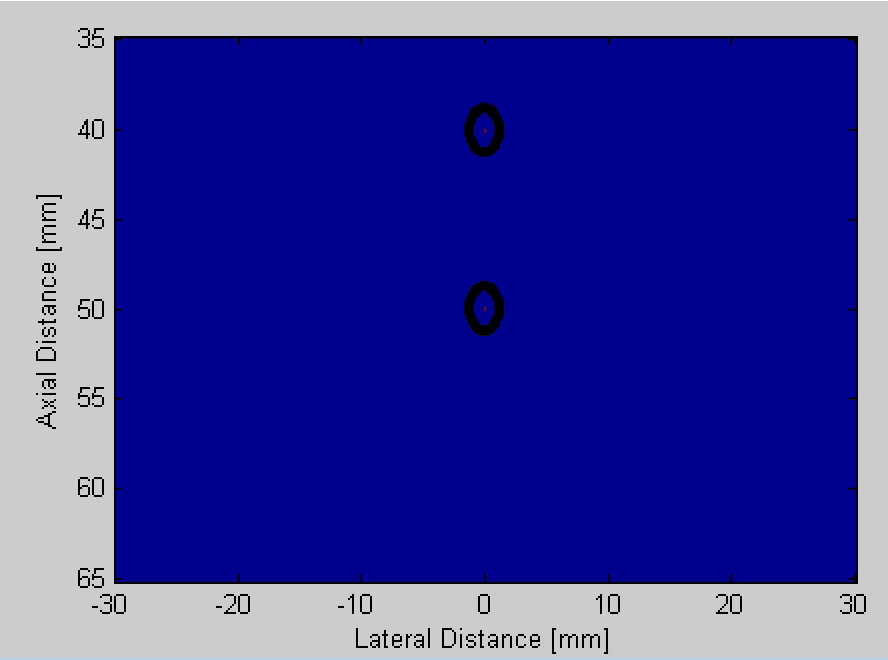

(a) 2-Point scatters based image truth

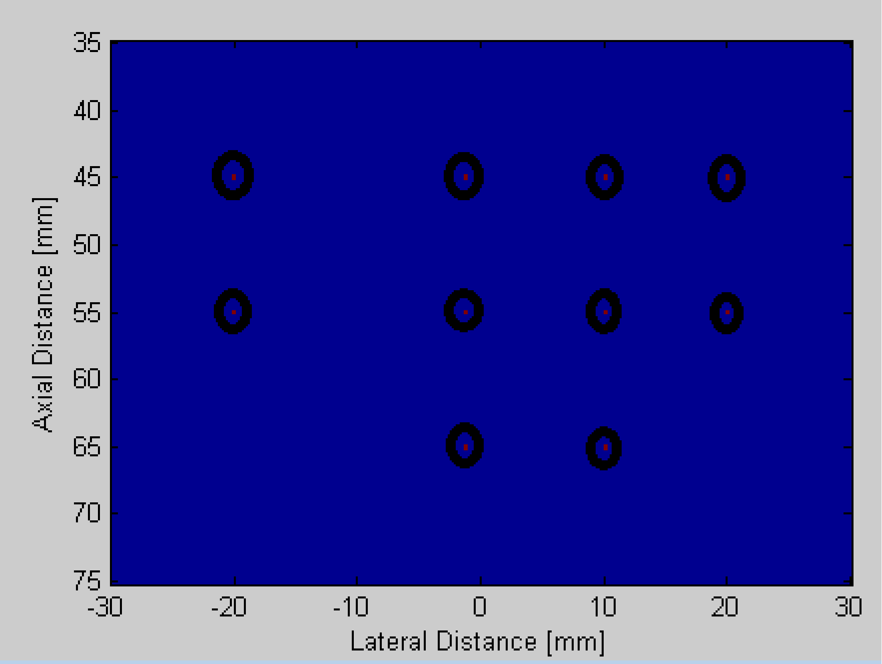

(b) 10-Point scatters based image truth.

Figure 2: Point scatter models implemented using Field II.

cysts. Figs. 4 and 5 represent more complicated scenarios based on phantoms for a kidney and a fetus within a human body.

For the 2-point target model (Fig. 2a), the region of interest is a (60 × 30) mm rectangle located 35mm below the transducer array. It is composed of 201 *x*-coordinates and 101 *z*-coordinates, which makes a total of 20301 grid points. The grid points start from −30mm to 30mm along the *x*-direction with a spatial spacing of 0.3mm. Similarly, the grid starts from 35mm to 65mm in the *z*-direction with spacing of 0.3mm. The two targets are located at (0, 40) mm and (0, 50) mm, respectively.

For the 10-point scatter model (Fig. 2b), the region is a (60 × 40) mm rectangle located 35mm below the transducer array. It is composed of 201 x-coordinates and 101 z-coordinates, which makes a total of 20301 scatter (reflector) points. The scatter points start from −30mm to 30mm along the *x*-direction with a horizontal spacing of 0.3mm and starts from 35mm to 75mm in the *z*-direction with a spacing of 0.4mm. The targets are located at (−20, 45) mm , (−20, 55) mm, (−1.2, 45) mm, (−1.2, 55) mm, (−1.2, 65) mm, (10.2, 45) mm, (10.2, 55) mm, (10.2, 65) mm, (20.1, 45) mm, and (20.1, 55) mm, respectively.

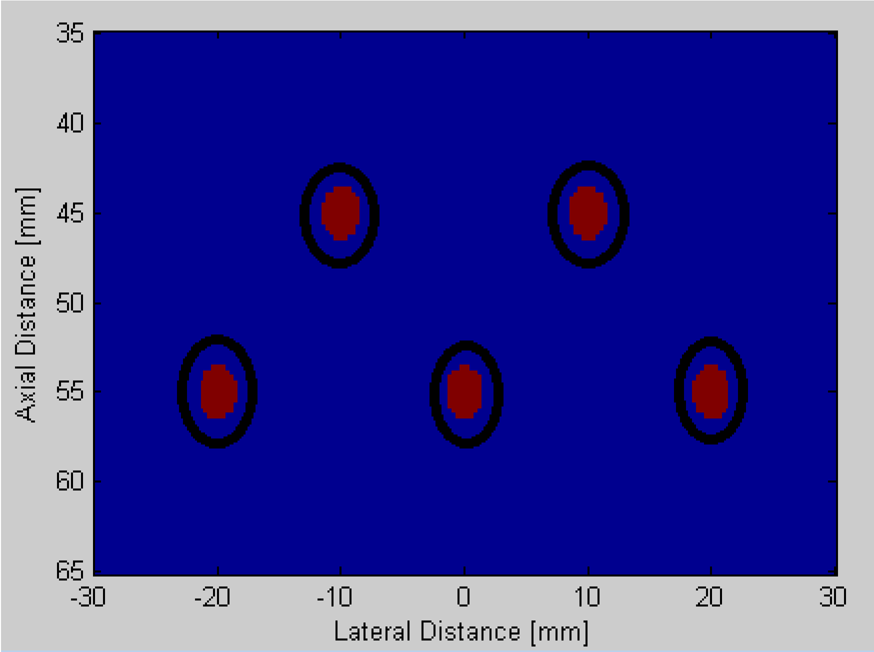

(a) 5-Cyst phantom image truth

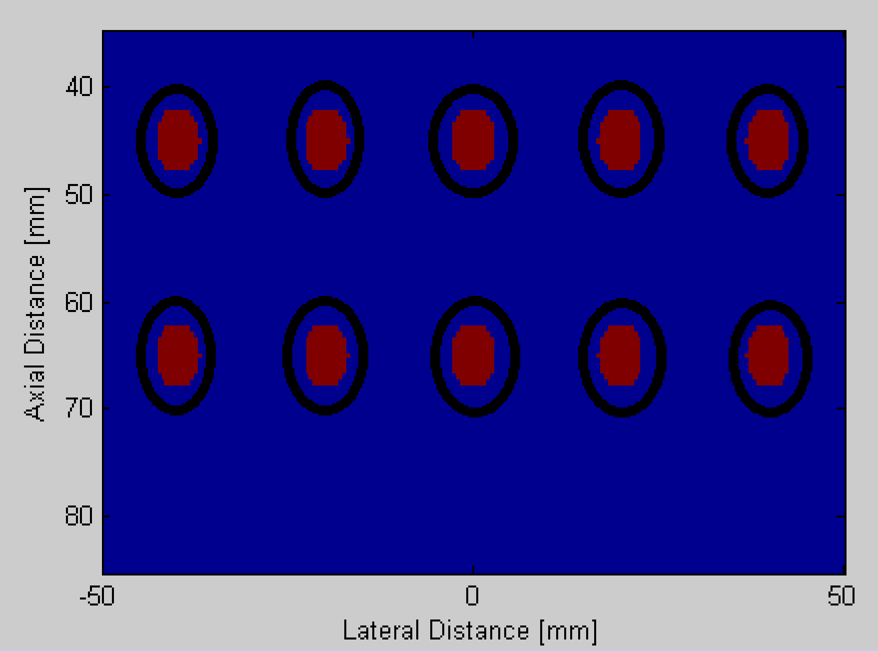

(b) 10-Cyst phantom image truth

Figure 3: Cyst models implemented using Field II.

The 5-cyst phantom model (Fig. 3a) is based on a rectangular region of (60 × 30) mm mm, located 35mm under the transducer array. It is composed of 201 *x*-coordinates and 101 *z*-coordinates, which makes a total of 20301 scatter (reflector) points. The scatter points start from −30mm to 30mm in the *x*-direction with a spacing of 0.3 mm and starts from 35mm to 75mm in the *z*-direction with a spacing of 0.4mm. The cysts are circular regions with radius of 1.5mm centered at (−10, 45) mm, (10, 45) mm, (–20, 55) mm, (0, 55) mm and (20, 55) mm.

The 10-cyst phantom model (Fig. 3b) comprises a rectangular region of (100 × 50) mm, located 35mm under the transducer array. It is composed of 201 *x*-coordinates and 101 *z*-coordinates, which makes a total of 20301 grid points. The grid points start from −50mm to 50mm in the *x*-direction with a spacing of 0.5 mm and starts from 35mm to 85mm in the *z*-direction with a spacing of 0.5mm. The cysts are circular regions with radius of 3mm centered at (–40, 45) mm, (–20, 45) mm, (0, 45) mm, (20, 45) mm, (40, 45) mm, (–40, 65) mm, (–20, 65) mm, (0, 65) mm, (20, 65) mm, and (40, 65) mm, respectively.

In Figs. 2 and 3, the parts circled in black are point/cysts targets which have the highest intensity in the region of interest. All other grid points have random

Gaussian intensities with a standard deviation of 0.01 except for the point/cyst scatters, which have intensities of 100.

Fig. 4 shows a phantom for a 3 months old fetus made up of 200,000 grid points, randomly distributed within the phantom. The phantom was scanned with a 64 element transducer array at a frequency of 5MHz. A rectangular region of (100 × 60) mm located 20mm under the transducer array is simulated using a scatter map, which is composed of 512 *x*-coordinates and 512 *z*-coordinates. The grid points start from –50mm to 50mm in the *x*-direction from 20mm to 80mm in the *z*-direction.

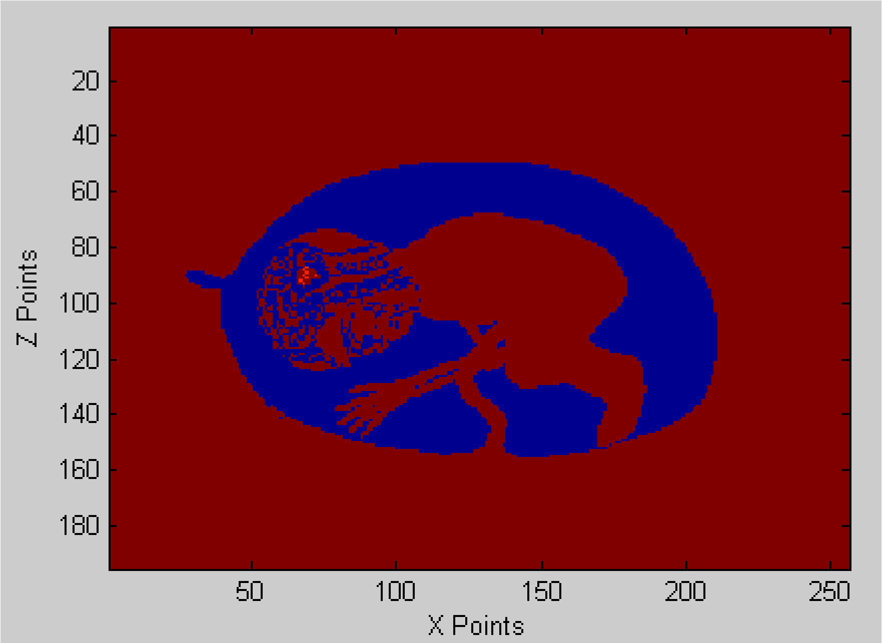

Figure 4: An example of the fetus phantom simulated using Field II.

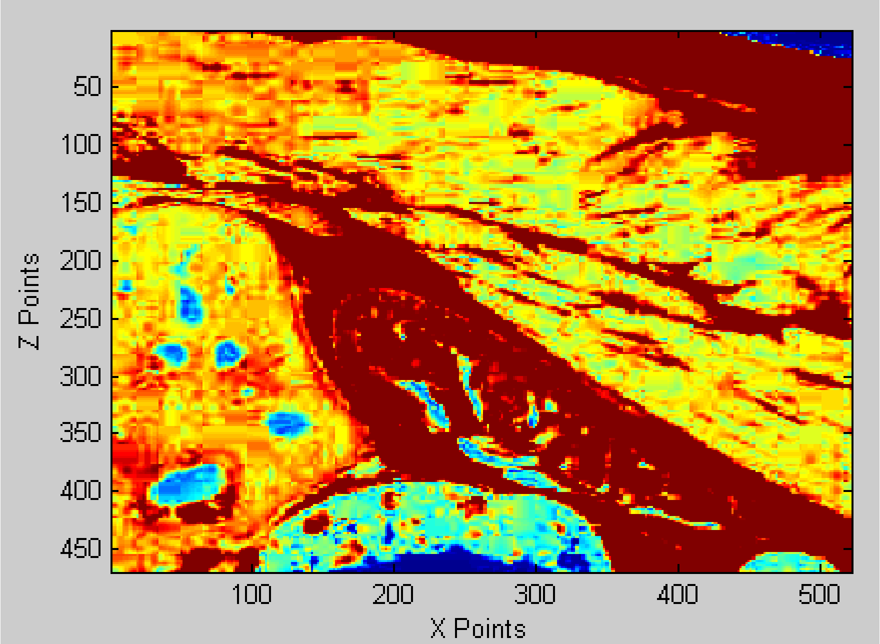

Figure 5: An example of the kidney phantom simulated using Field II.

Figure 5 shows a phantom for the left kidney constructed using 1,000,000 scatter points randomly distributed within the phantom. The phantom was scanned with a 128 element transducer array at 7MHz. A rectangular region of (100 × 85) mm located 20mm under the transducer array is simulated using a scatter map, which is composed of 512 *x*-coordinates and 512 *z*-coordinates. The scatter points start from −50mm to 50mm in the *x*-direction and from 20mm to 105mm in the *z*-direction.

2.2 Beamforming Algorithms

With Field II, each transmit element probes the region of interest one after the other and the backscatters for each probe is recorded by all receiving elements. With an M-element transducer the recorded signals can therefore be arranged in a $(M \times M)$ matrix. For a high quality image, we use all the $(M \times M)$elements of the observed matrix in the beamforming algorithms.

The following section explains how the two beamforming algorithms, namely the Delay-and-Sum and Capon algorithms, process the M backscattered signals to yield the beamformed image showing the differences in the performance of each algorithm.

2.2.1 Delay and Sum Beamforming Algorithm

The Delay-and-Sum (DAS) beamforming algorithm is a technique based on constructive and destructive interference. Each received signal at a transducer element is delayed by the duration corresponding to the time it takes for a backscatter to arrive from the reference pixel to the transducer element. The delay is, therefore, proportional to the distance between the reference pixel and the transducer element. After delaying all signals, they are added for each pixel. Fig. 6 represents the DAS algorithm for one pixel within the region of interest.

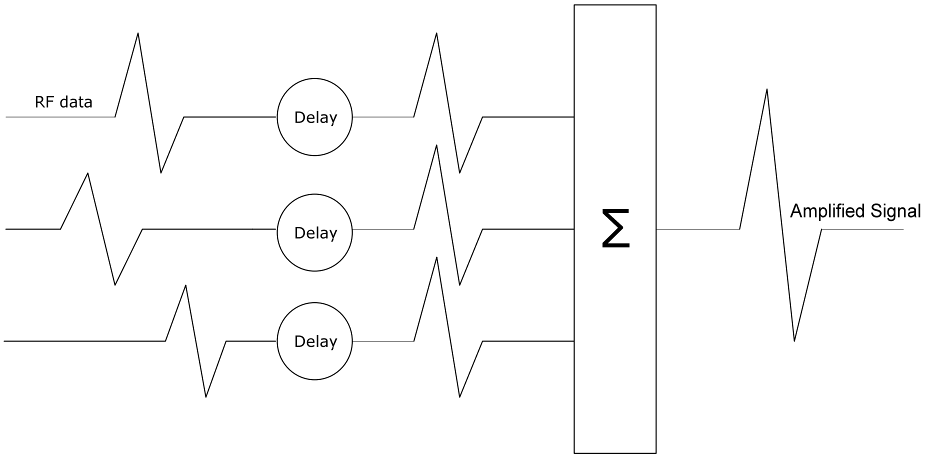

Figure 6: Block diagram illustrating the principal of the DAS beamformer.

For an *M*-element array, the equations below show how the beamformed signal for each scatter point is computed. Assuming x_m is the signal observed at element *m* of the transducer array, we get

$$r_{m,p} = \sqrt{\left(X_p - X_m\right)^2 - \left(Z_p\right)^2}\,, \tag{1.1}$$

$$D_{m,p} = 2 * r_{m,p} * \frac{F_s}{c}, \tag{1.2}$$

and $$BF_p[N] = \sum_{m=0}^{M-1} x_m[N - D_{m,p}], \tag{1.3}$$

where $r_{m,p}$ is the distance between the reference pixel *p* and transducer element *m*. Since the imaging scene is a 2D model so the *x* and *z* components of the transducer elements and the grid points (pixels) have to be taken into consideration. Notation

X_p and Z_p are the x and z components of the reference pixel, respectively. Since the transducer array is located on the x-axis, the z component of the transducer element is always zero and its x component is X_m. Symbol $D_{m,p}$ is the time delay between the reference pixel p and transducer element m in terms of the number of samples. BF_p denotes an array of length N showing the beamformed signal for pixel p. Finally, symbol

$$I_p = \sum_{\substack{i=10 \\ -\max(BF_p)}}^{10+\max(BF_p)} BF_p\,[i]\,, \tag{1.4}$$

where I_p is the intensity value of the pixel p, which shows the location of the high scattering regions in the image.

The DAS algorithm is independent of the second order statistics of data, therefore, the side lobes are high and the algorithm is very sensitive to the transducer location. The Capon beamforming algorithm will be explained in the next section that overcomes these limitations of the DAS algorithm.

2.2.2 Capon Algorithm

Capon beamforming relies on wave propagation and phase relationships. Using the principals of superimposing waves, a higher or lower amplitude wave is created (e.g., by delaying and weighting the signal received). The Capon beamforming system dynamically adapts in order to maximize or minimize a desired parameter, such as the signal to noise ratio (SNR) [3] – [6].

Using the same setup and notation as was used for the DAS beamformer, the output using the Capon beamformer is given by [7] – [8]

$$z_p[N] = \sum_{m=0}^{M-1} w_p[N] x\_delayed_m[N], \tag{1.5}$$

$$x_{delayed[N]} = \left[x_0\left[N - D_{0,p}\right], x_1\left[N - D_{1,p}\right], \quad \ldots, x_{M-1}\left[N - D_{M-1,p}\right]\ \right]^T, \tag{1.6}$$

and w_p is the time-varying weight at scattering point p. The Capon beamformer works by minimizing the variance of $z_p[N]$ given by

$$\min_{w_p[N]} E\left[\left|z_p[n]\right|^2\right] = \min_{w_p[N]} w_p[n]^H R[n] w_p[n]$$

$$\text{subject to } w_p[n]^H a = 1 \tag{1.7}$$

where $E[.]$ is the expectation operator. The sample covariance matrix is computed as $R_p[n] = E[x\_delayed[n]\ x\_delayed[n]^H]$ and symbol a denotes the steering vector. Since the data has already been pre-beamformed then a is simply a vector of ones. The analytical solution [8] for Eq. (1.7) is given by

$$w_p[N] = \frac{R_p[N]^{-1}\boldsymbol{a}}{\boldsymbol{a}^H R_p[N]^{-1}\boldsymbol{a}}. \tag{1.8}$$

After applying the weights to Eq. (1.5), the beamformed intensity of each scattering point p is $I_p = \max(z_p[N])$.

2.3 Results of DAS Vs. CAPON algorithms

In this section, the results of the DAS algorithm are compared with those obtained from the Capon beamformer at a SNR of 40dB for all of the simulation environments presented in Section 1.1. I illustrate the difference in the performance of both algorithms especially when environment gets complicated as is the case for the cyst phantoms.

In order to quantitatively compare the resulting images, we used structural similarity (SSIM) index, commonly used for measuring the similarity between two images [9]. The SSIM index can be viewed as a quality measure of one of the images in comparison to another image that is regarded to be of perfect quality. The higher the SSIM, the higher is the similarity between the two images. The maximum value of SSIM is, therefore, 1 representing perfect alignment.

All the SSIM values calculated in the images below are between the image truth and the beamformed image using either the DAS or Capon algorithm.

Images for 2-Point Scatters:

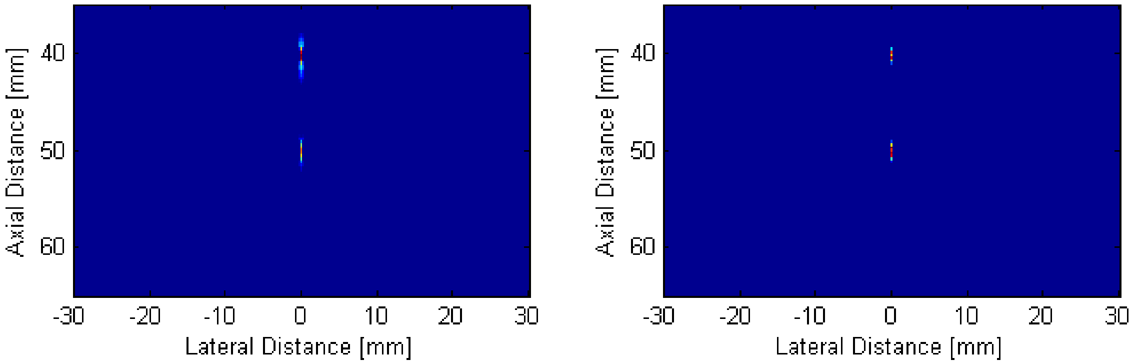

(a) DAS Algorithm,
SSIM = 0.9289

(b) CAPON Algorithm,
SSIM = 0.9615

Figure 7: Beamformed Images for the 2-point scatter using (a) DAS algorithm, (b) CAPON algorithm

Images for 10-Point Scatters:

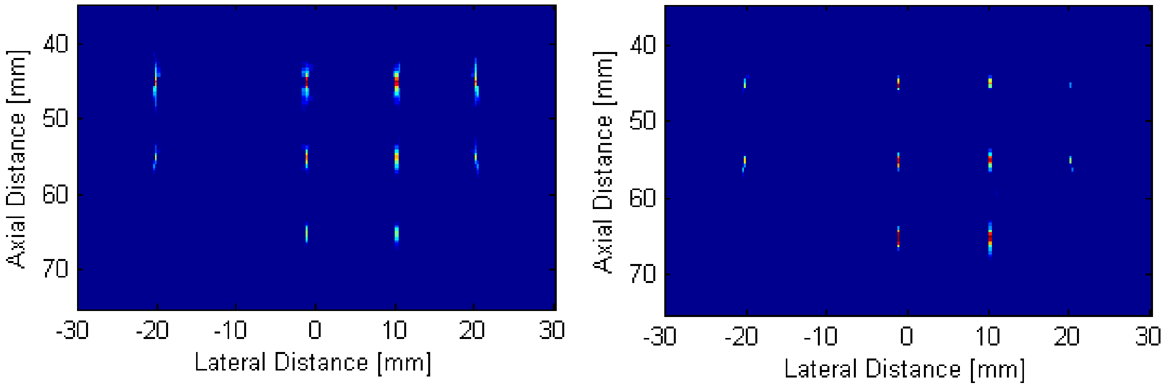

(a) DAS Algorithm,
SSIM = 0.7194

(b) CAPON Algorithm,
SSIM = 0.7630

Figure 8: Beamformed Images for the 10-point scatter using: (a) DAS algorithm, and (b) CAPON algorithm.

Images for 5-Cysts Phantom:

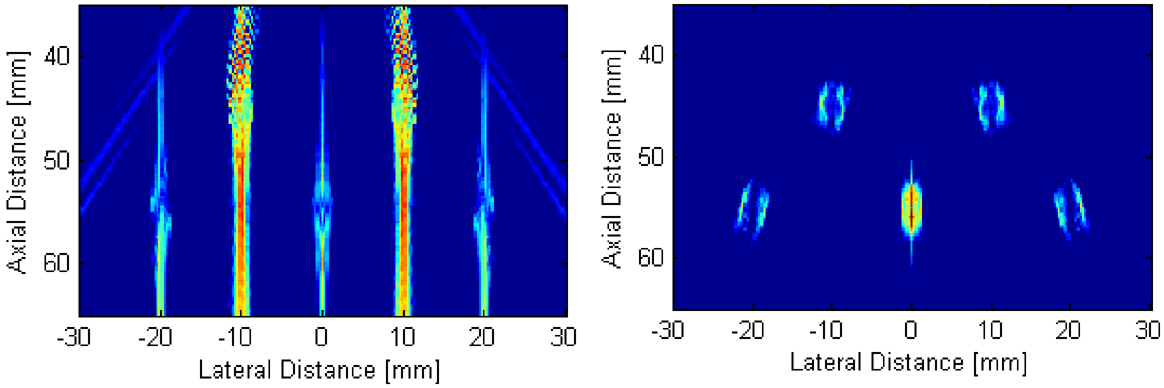

(a) DAS Algorithm,
SSIM = 0.2096

(b) CAPON Algorithm,
SSIM = 0.7727

Figure 9: Beamformed Images for the 5-Cyst phantom using: (a) DAS algorithm, and (b) CAPON algorithm.

Images for 10-Cysts Phantom:

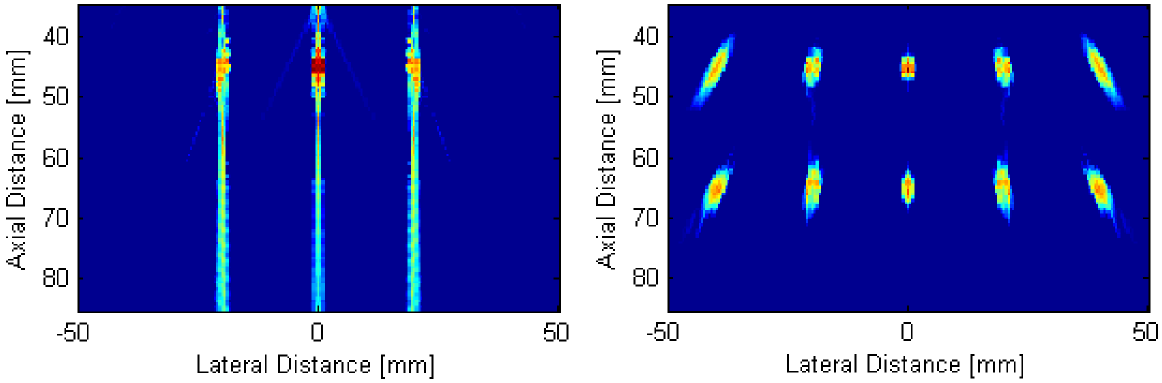

(a) DAS Algorithm,
SSIM = 0.1099

(b) CAPON Algorithm,
SSIM = 0.6841

Figure 10: Beamformed Images for the 10-Cyst phantom using: (a) DAS algorithm, and (b) CAPON algorithm.

As seen from the images above, the Capon beamforming is performing much better reconstruction than the DAS beamforming algorithm, especially for more complicated environments. For each image, the SSIM value is calculated with respect to the image truth. In all cases, the Capon algorithm has a higher value of SSIM as compared to the DAS algorithm illustrating the superiority of the Capon beamformer. The superior performance of the Capon beamformer is also evident from the perceptual quality of the reconstructed images.

Chapter 3
Introduction to Compressive Sensing

To achieve clarity in the reconstructed image, an ultrasound machine uses a large number of transducer elements to collect the backscatter reflections. This leads to a large amount of data when the backscatter reflections are sampled at the classical Nyquist rate, i.e., at twice the maximum frequency present in the recorded signal. To prevent aliasing and for perfect reconstruction, the Shannon/Nyquist theorem states that the minimum sampling rate of a signal should be $2W$ samples/second (where W is the highest frequency of the signal). The notion behind compressive sensing (CS) is to sample the signals at a rate below the Nyquist rate and still produce a reconstructed signal of reasonable quality CS offloads the memory requirements from the signal acquisition stage to signal reconstruction stage which gives an advantage of fast data acquisition. Moreover, it reduces the processing speed of the analog to digital converter which is the most expensive part in the ultrasound machine since less amounts of data are being acquired. CS exploits the fact that the signal is sparse in a certain domain and, therefore, has a concise representation. Chapter 3 introduces CS and applies it to the ultrasound signals with sparse representation.

3.1 What is Compressive Sensing?

As previously mentioned, CS is based on the notion that a small number ofmeasurements of a **compressible** signal contains enough information for reconstruction and processing of the signal.

In this thesis, we apply CS to raw radio frequency (RF) data, obtained as backscatters from simulated human tissues. The data received at each transducer element has N samples. We want to reconstruct these N samples from only M samples using CS. Beamforming is then applied to reconstruct the image using the reconstructed RF data, [10]–[11], [21]. Fig. 11 shows the various steps used in the CS calculations.

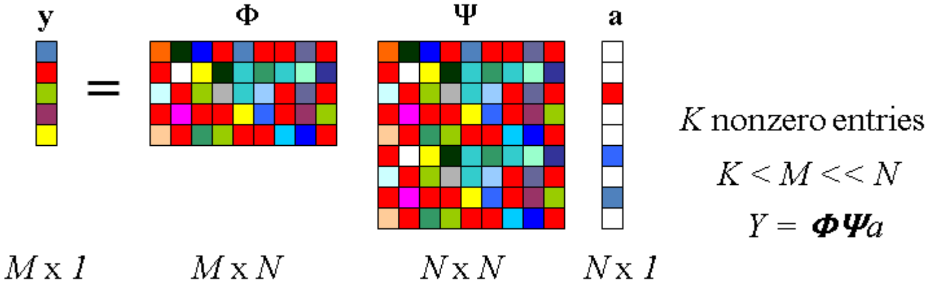

Figure 11: Schematic diagram representing compressive sampling.

In summary, in order to apply CS to RF signals we need:

- Prior knowledge that the data has sparse representation in some basis Ψ.
- CS dictionary, which is incoherent with the basis function Ψ.

- Appropriate sensing matrix Φ, which is guaranteed by randomness.
- Optimization for recovering the signal.

The sensing matrix Φ is designed such that the sparse signal a can be recovered exactly from a reduced number of measurements y. This can be achieved by using a sensing matrix, which is highly incoherent to the basis matrix Ψ. Using a random matrix, we are able to closely reconstruct the k-sparse vector a with high probability with just $M \geq Klog\left(\frac{N}{K}\right)$ random measurements. Note that the notation k is the number of non-zero entries in the sparse vector a. Sensing matrices will be explained further in Section 2.2.

As for the basis matrix, we use the waveatom transform, which represents the time-dependent Green's function in a tight frame of multi-scale, directional wave packets. Briefly, waveatom is the transform that finds the exact relationship between the directional wavelets and the Gabor transform in the sense that the period of the oscillations of each wave packet is linked to the size of the essential support region of the parabolic scaling wavelength wavelength ~ $(\text{diameter})^2$.

The name Waveatom comes from its inherent property of providing an optimally sparse representation of wave propagators [12]–[14].

For simplicity, wave atoms below are defined for α =β =1/2, where α indexes the multiscale nature of the transform. From α = **0,** which is considered uniform can range to **1,** which is considered dyadic. Parameter β measures the wave packet's directional selectivity, where **0** and **1** indicate best to poor selectivity.

In one dimension (1D), the wave atoms formulation is defined as follows. Consider *f(x)* and *f (w)* as a 1D Fourier transform pair, *x* and *w* correspond to the coordinates in the time domain and the frequency domain, respectively. Define wave atoms as $\varphi_\mu(x)$, where $\mu = (j, m, n)$. Then the indexed point (x_μ, ω_μ) in the phase-space domain is defined by [22]-[23]:

$$x_\mu = 2^{-j}m \quad and \quad \omega_\mu = \pi 2^j n$$

The elements of φ_μ are called Waveatoms and have the values

$$|\hat{\varphi_\mu}(\omega)| \leq C_M 2^{-j}(1 + 2^{-j}|\omega - \omega_\mu|)^{-M} + C_M 2^{-j}(1 + 2^{-j}|\omega + \omega_\mu|)^{-M}$$

and $|\varphi_\mu(\omega)| \leq C_M 2^j (1 + 2^j |x - x_\mu|)^{-M}$ for all M > 0.

Section 2.3 shows the difference between reconstructed signals using waveatom basis versus the discrete cosine transform (DCT) basis.

The last step in CS is the recovery of the signal a. Since $M < N$, the reconstruction is ill-conditioned and there are infinitely many Ψ such that $y =$

$\Phi\Psi a$. So, the recovery of the signal must be done by solving the minimization problem [5] given below

$$\hat{a}_1 = \arg\min_{a} \{ ||a||_1 \text{ such that } y = \Phi\Psi a \} \tag{2.1}$$

Once the signal a is recovered, we can apply the inverse of the basis Ψ to obtain the original RF signal.

In the following two sections, the sensing and basis matrices will be explained. In each case, the root mean squared error (RMSE) between the original and reconstructed RF signals are calculated based on the formula

$$RMSE = \sqrt{\frac{\sum_{i=1}^{N}(x_i - \hat{x}_i)^2}{N}} \tag{2.2}$$

to compare the quality of reconstruction. In Eq. (2.2), notation x_i and $\hat{x}_i$ represent the original and reconstructed signals respectively and *N* is the total number of samples within a signal.

3.2 Sensing Matrices

The sensing matrix Φ is designed such that sparse/compressible signals can be recovered exactly from the measurements *y*. This can be achieved by using a sensing matrix, which is highly incoherent to the sparse representation achieved by matrix Ψ. In order to identify samples that are not all zeros with high probability, we need a sensing matrix where the samples have dense representation. This is achieved by choosing a matrix that is “not similar” or incoherent to the sparsity inducing matrix **Φ**. Using random matrices, we are able to perfectly reconstruct sparse vectors with high probability with $M < N$ random measurements since it is experimentally proven that fixed basis are highly incoherent with random matrices. Furthermore, the measurement process is non-adaptive, so that the sensing matrix Φ does not depend in any way on the input RF signals.

3.2.1 Binary Sensing Matrices

The first type of sensing matrices used is the binary sensing matrix, where all row entries of Φ are zeros except for one, where location is chosen randomly. It has the value of one. Therefore, the resulting decimation factor for each RF signal is M.

Fig. 12 shows the comparison between the original and reconstructed data using 90% subsampling rate with the binary sensing matrix for the signal received at one transducer element for a 5-Cysts phantom. A 90% subsampling rate implies that only 10% of the original samples are maintained in vector y. In Fig. 12, I selected a backscatter waveform recorded at the transducer element, applied compressive sensing by randomly picking only 10% of the samples, and then reconstructed the signal by solving the optimization problem, Eq. (12). The resulting RMSE is 0.5646.

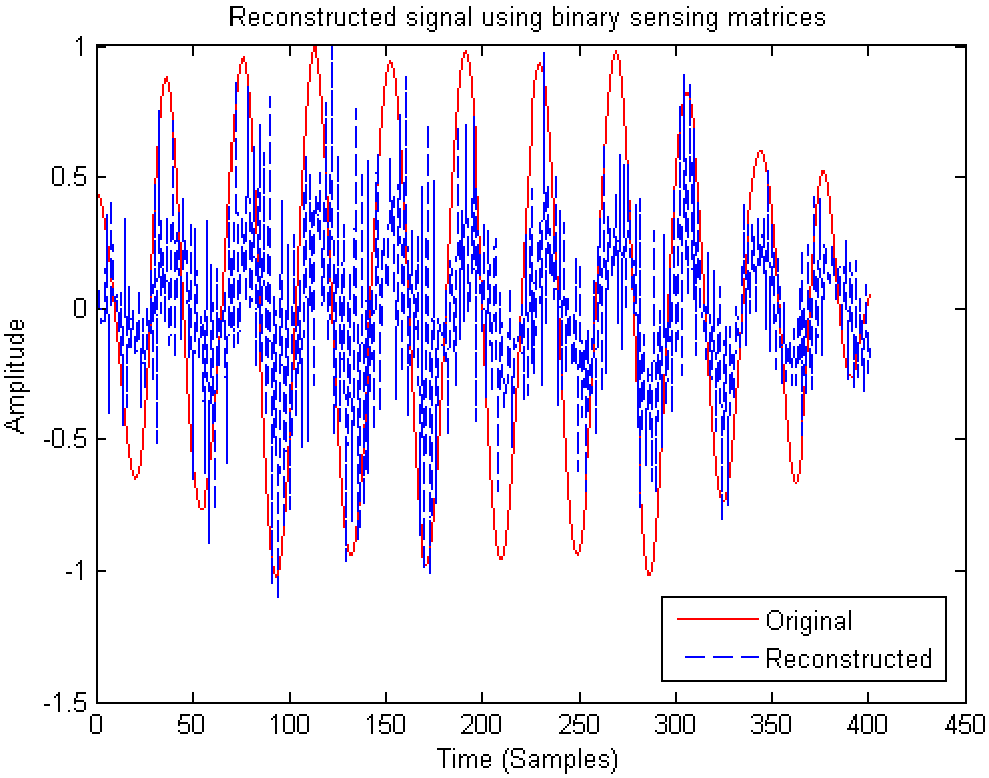

Figure 12: Signal reconstructed using the binary sensing matrix versus the original signal

3.2.2 Bernoulli Sensing Matrices

Assuming that *Φi,j* is the *i*'th row, *j*'th column entry of the Hadamard matrix. We generate a new matrix by removing all negative values in the Hadamard matrix and name the resulting matrix as the semi-Hadamard matrix with the form [15]:

$$\phi_{i,j} = \begin{cases} 2/\sqrt{M} & h_{i,j} = 1 \\ 0 & h_{i,j} = -1 \end{cases} \tag{2.3}$$

The semi-Hadamard matrices are a special kind of binary matrices, which preserve the binary performance in CS. Fig. 13 compares the original and reconstructed signals using 90% subsampling rate with the Bernoulli sensing matrix for the signals recorded at a transducer element for a 5-Cysts simulation. The resulting RMSE is 0.1248, which is less than the one obtained from the binary sensing matrix. Therefore, the Bernoulli sensing matrix provides superior performance than the binary sensing matrix.

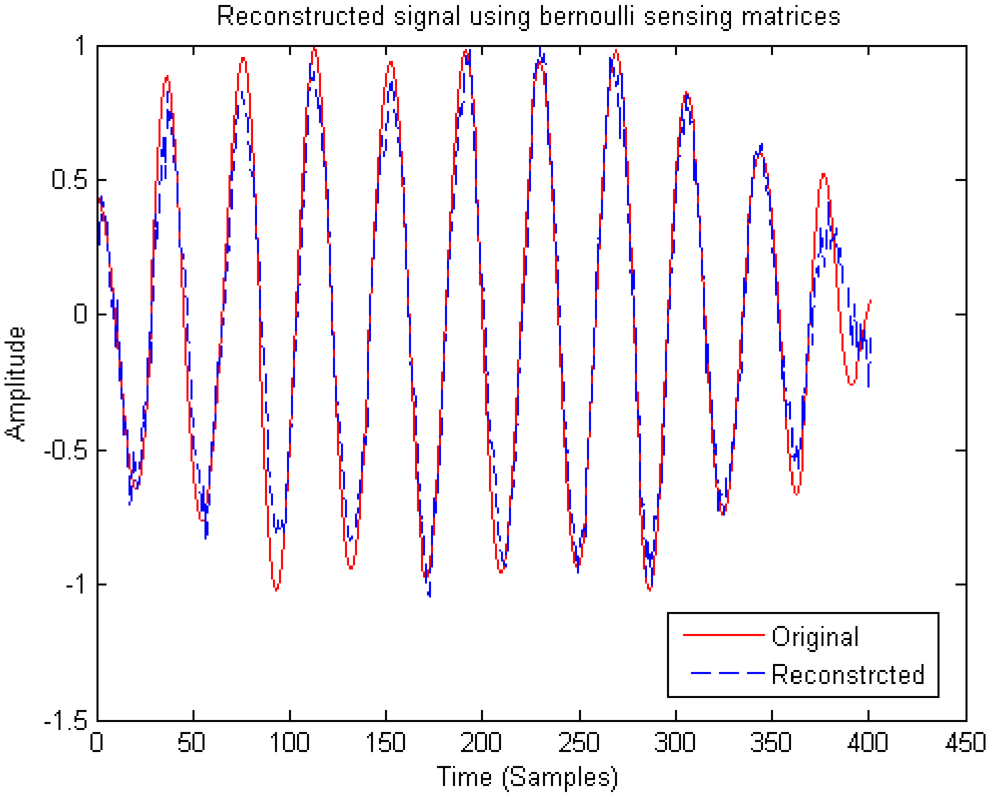

Figure 13: Signal reconstructed using the Bernoulli sensing matrix versus the original signal

3.3 Basis Matrices

The quality of the CS reconstruction depends on the sparsity of the data. Due to the oscillatory pattern of the RF data in ultrasound, it is difficult to find a sparse representation in any basis. We tried different basis functions and came to the conclusion that the wavetom transform (WAT) results in much higher performance compared to the the discrete cosine transform (DCT). Figs. 14 and 15 shows the difference between the quality of reconstructed signals using the DCT and WAT basis using 90% subsampling rate. In each simulation, the Bernoulli sensing matrix is applied to the signal recorded at one transducer element for a 5-cyst phantom. The resulting RMSE for the DCT basis function is 6.6425 and for the waveatom basis function is 0.3443.

As can be seen from the figures below, the WA basis works much better than the DCT basis.

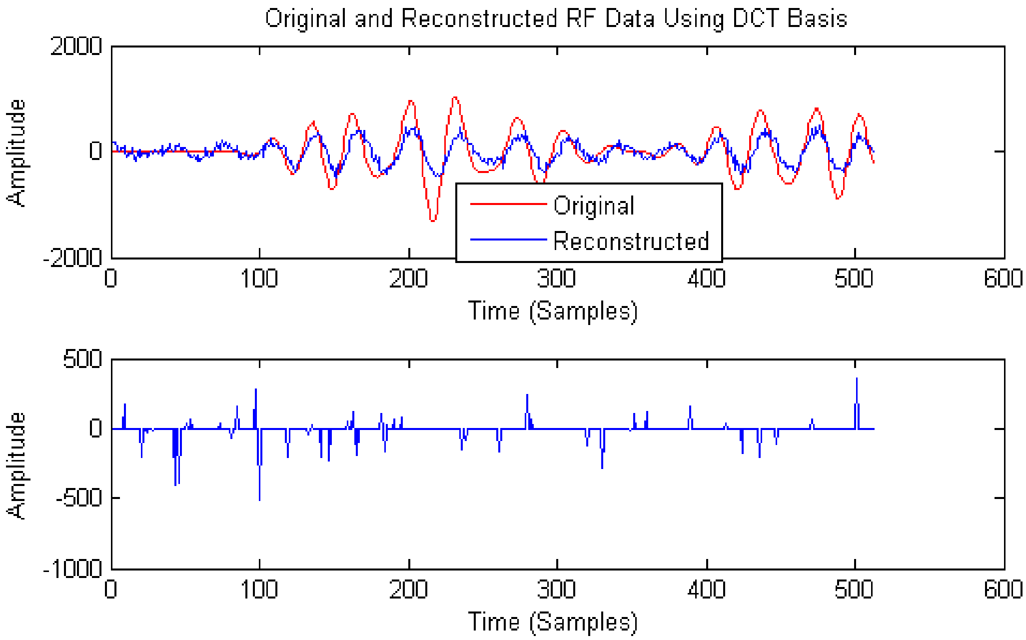

Figure 14: Reconstruction using the DCT basis function.

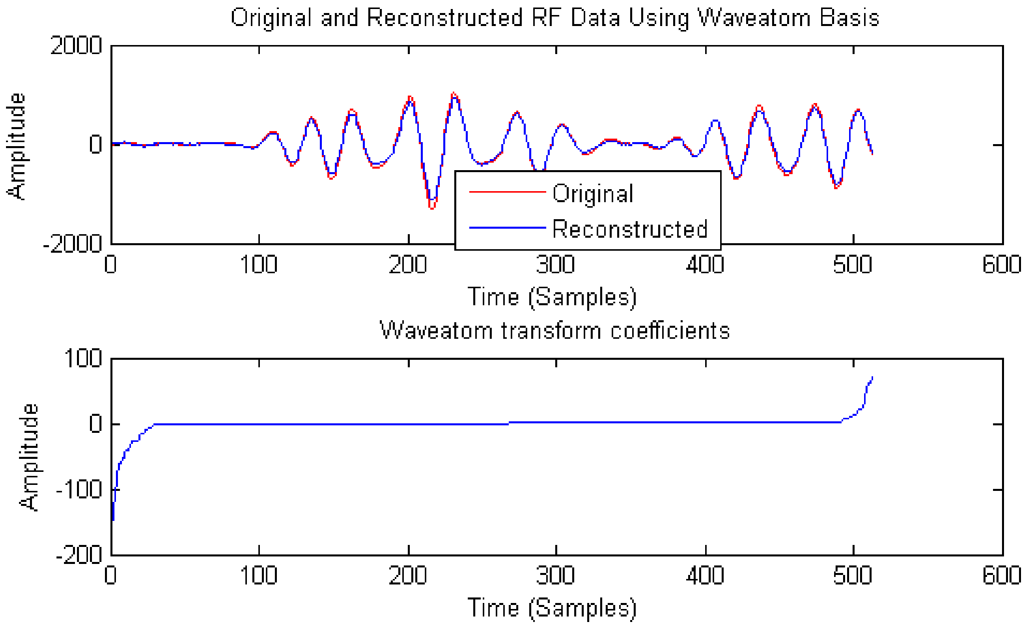

Figure 15: Reconstruction using the WA basis function.

3.4 Compressive Sensing Results

This section shows the beamformed images obtained after applying CS on the raw RF signals for each of the models presented in Chapter 2. Namely, the models considered are:

1. 2-point scatter simulation.
2. 10-point scatter simulation.
3. 5-cyst phantom simulation.
4. 10-cyst phantom simulation.
5. Fetus phantom simulation.

6. Kidney phantom simulation.

The recorded elements at the transducer elements are compressed using different decimation factors, ranging from 4 to 10. Recall that the decimation factor is the fraction of original samples retained for reconstruction. Lesser the number of samples retained, worse is the reconstruction in the beamformed image.

As explained in Chapter 2, for an M element transducer array the recorded signals can be arranged in a $(M \times M)$ matrix. The previous chapter showed the BF images using the all the $(M \times M)$ recorded signals. To provide additional saving in the computational time, the beamformed images presented in this chapter use only the diagonal entries. In the next chapter, we compare these images with images obtained from a combination of compressive sensing and time reversal. The later technique is specially beneficial in environment with rich multipath that adversely affects the performance of compressive sensing.

We use a Bernoulli random sensing matrix to reduce the sampling rate by the selected decimation factor. For sparse representation, a waveatom basis is used. Generally speaking, waveatoms interpolates between directional wavelets and Gabor. An optimization problem based on regularized l1-norm is solved, as given in Eq. (2.1), and used to reconstruct the signals. Finally, the reconstructed signals are beamformed using the Capon algorithm. The block diagram representation of the process used to derive the results in this section is given in Fig. 16. In order to show how well compressive sensing works, the images using original RF data with diagonal entries and the images using the reconstructed RF data were compared using the structural similarity (SSIM) index assuming the images obtained using the original RF data are of perfect quality.

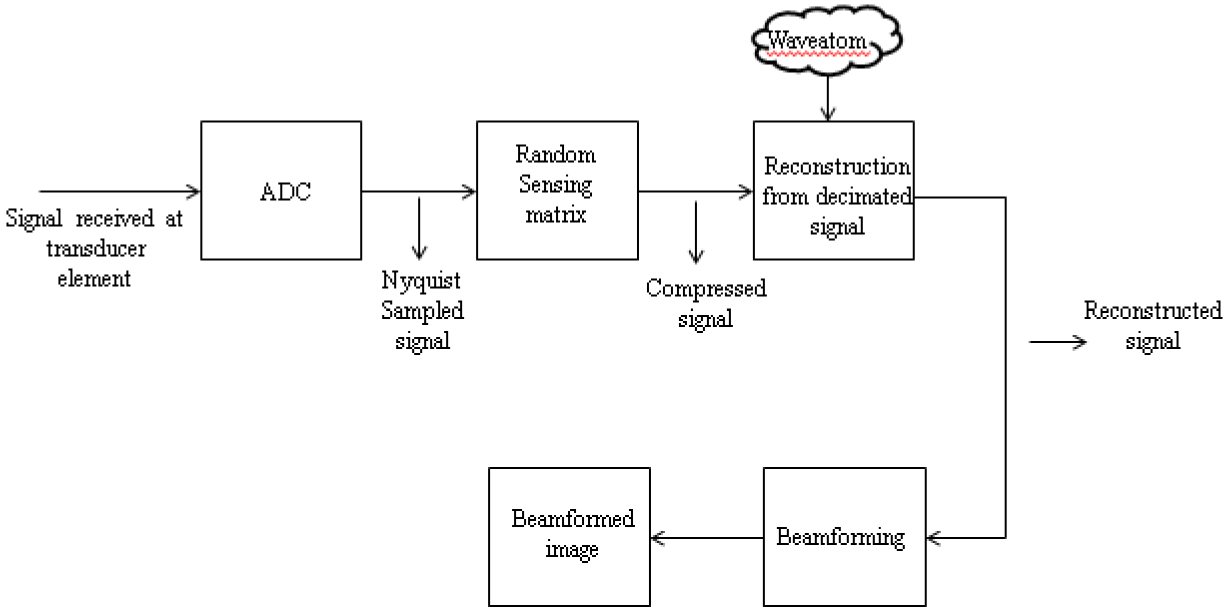

Figure 16: Implementation block diagram for compressive sensing.

Besides the SSIM index, another parameter used to quantitatively assess the quality of reconstructed images is the Mean Absolute Error (MAE) in dBs between the two images, which is defined as,

$$MAE = \frac{1}{D}\sum_{i=1}^{D}|I\_Original_i - I\_Reconstructed_i| \tag{2.4}$$

where D is the total number of pixels in the 2D image, while $I\_Original_i$ and $I\_Reconstructed_i$ are the intensities of the beamformed images reconstructed using the original and reconstructed RF data, respectively.

Images using Reconstructed RF data:

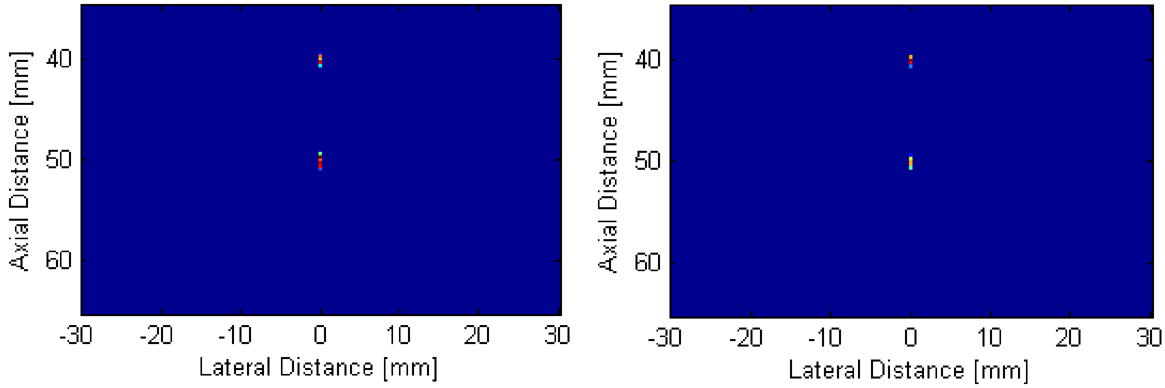

(a) Beamformed Image with original RF data using the diagonal entries only.

(b) Beamformed Image with decimation factor 4: SSIM = 0.9966, MAE = -7.5507 dB.

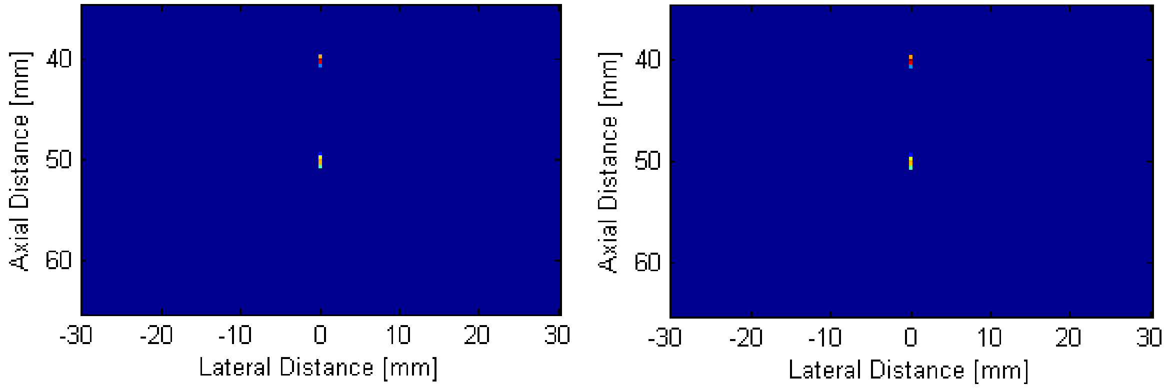

(c) Beamformed Image with decimation factor 6: SSIM = 0.8752, MAE = 7.5531 dB

(d) Beamformed Image with decimation factor 10:SSIM = 0.8760, MAE = -7.5652 dB

Figure 17: Beamformed image reconstructed from decimated data for the 2-point scatter simulation: (a) Image using original diagonal data; (b) Decimation factor of 4; (c) Decimation factor of 6; (d) Decimation factor of 10.

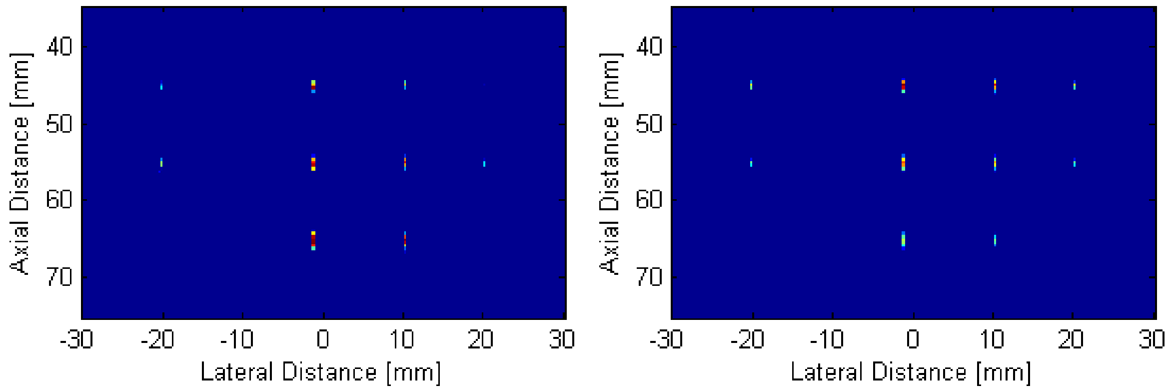

(a) Beamformed Image with original RF data using only diagonal entries

(b) Beamformed Image with decimation factor 4: SSIM = 0.9845, MAE = -2.3349 dB

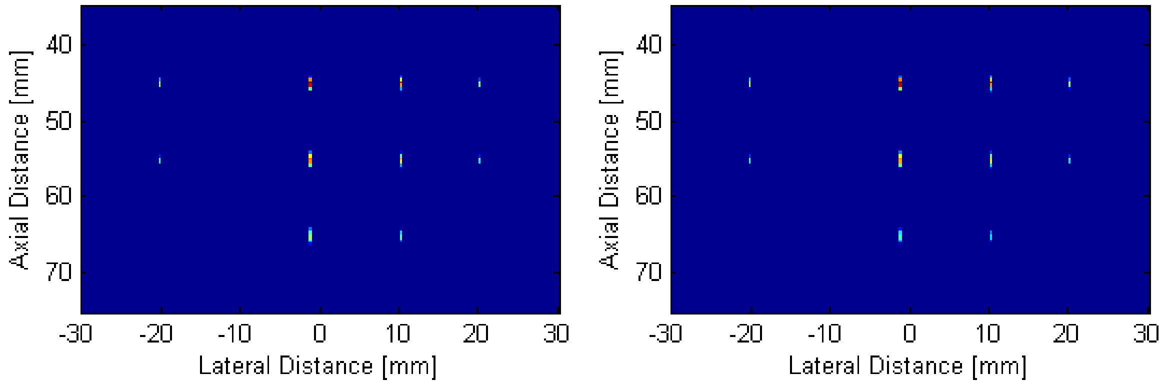

(c) Beamformed Image with decimation factor 6: SSIM = 0.9836, MAE = -2.2205 dB

(d)Beamformed Image with decimation factor 10: SSIM = 0.8099, MAE = -1.6471 dB

Figure 18: Beamformed image reconstructed from decimated data for the 10-point scatter simulation: (a) image using original diagonal data; (b) Decimation factor of 4; (c) Decimation factor of 6; (d) Decimation factor of 10

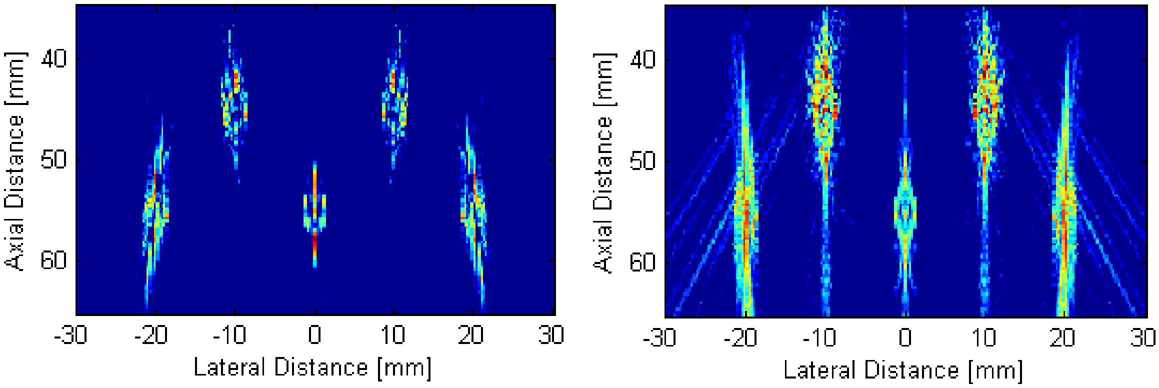

(a) Beamformed Image with original RF data using only diagonal entries

(b) Beamformed Image with decimation factor 4: SSIM = 0.9021, MAE = 6.3051dB

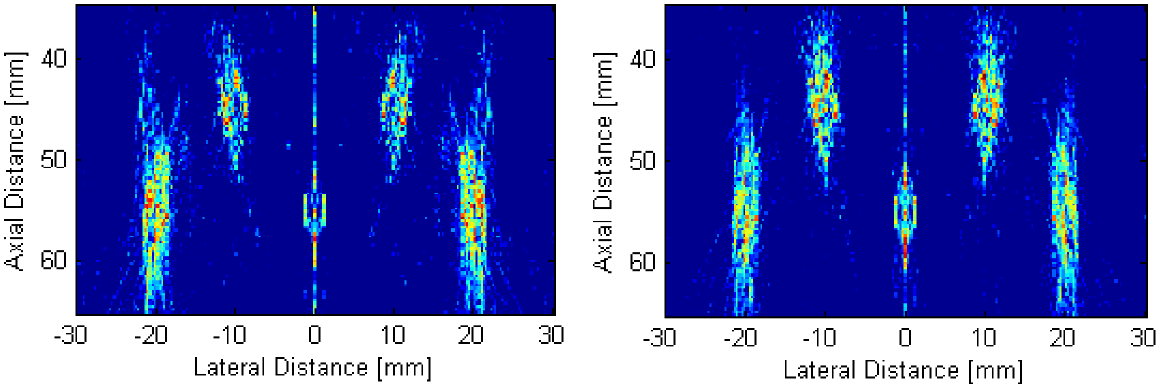

(c) Beamformed Image with decimation factor 6: SSIM = 0.8871, MAE = 5.9761 dB

(d) Beamformed Image with decimation factor 10: SSIM = 0.8475, MAE = 6.6332 dB

Figure 19: Beamformed image reconstructed from decimated data for the 5-cyst phantom simulation: (a) image using original diagonal data; (b) Decimation factor of 4; (c) Decimation factor of 6; (d) Decimation factor of 10.

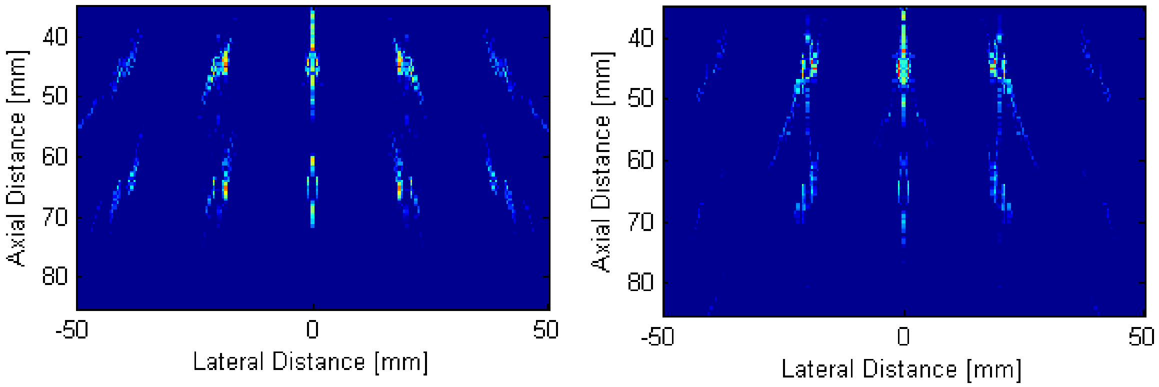

(a) Beamformed Image with original RF data using only diagonal entries

(b) Beamformed Image with decimation factor 4: SSIM = 0.8790, MAE = 3.9407 dB

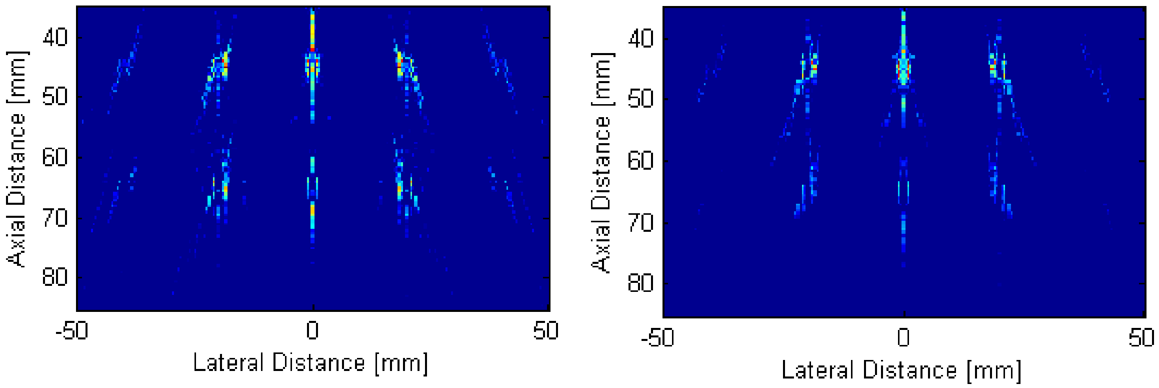

(c) Beamformed Image with decimation factor 6: SSIM = 0.8653, MAE = 4.3544 dB

(d) Beamformed Image with decimation factor 10: SSIM = 0.6753, MAE = 5.2335 dB

Figure 20: Beamformed image reconstructed from decimated data for the 5-cyst phantom simulation: (a) image using original diagonal data; (b) Decimation factor of 4; (c) Decimation factor of 6; (d) Decimation factor of 10.

Figs. 17, 18, 19 and 20 show the effect of applying CS to RF data using simple and complicated environments, the figures show that the higher the signal decimation factor, the lower is the SSIM and the higher is the MAE value between the image obtained using the original and reconstructed RF data. Figs. 21 and 22 shows how well CS works with real body parts such as the fetus and kidney phantoms presented earlier.

3.5 Summary

In summary, compressive sensing is applied on signals received at each transducer element. Each signal of length *N* is reconstructed from only *M* samples using Bernoulli matrix for the sensing and waveatoms for the basis matrix for optimum signal reconstruction. The full length reconstructed signal is processed using the Capon beamforming algorithm to yield the 2D image of the scene. Results show that signal reconstruction is successful with subsampling up to 90% for point, cyst, fetus and kidney phantoms.

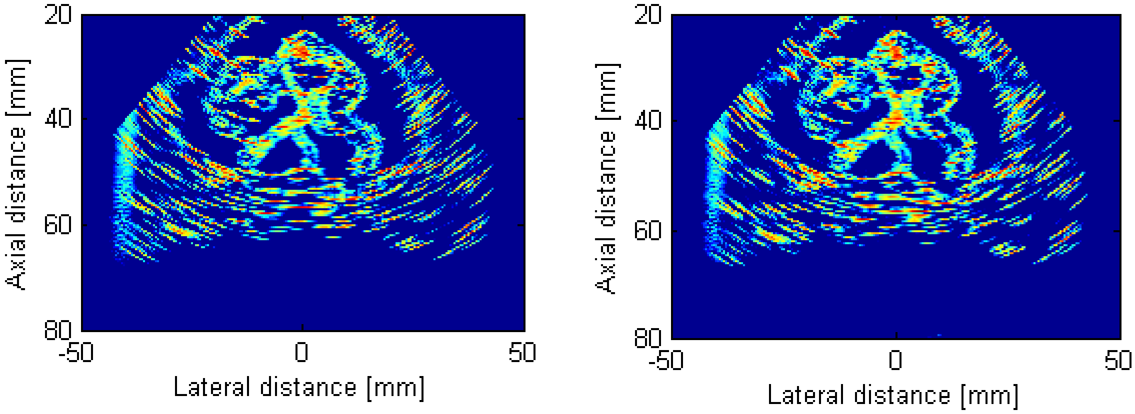

(a) Beamformed Image for Fetus Phantom using original RF data

(b) Beamformed Image with decimation factor 4: SSIM = 0.9710, MAE = 5.2768 dB

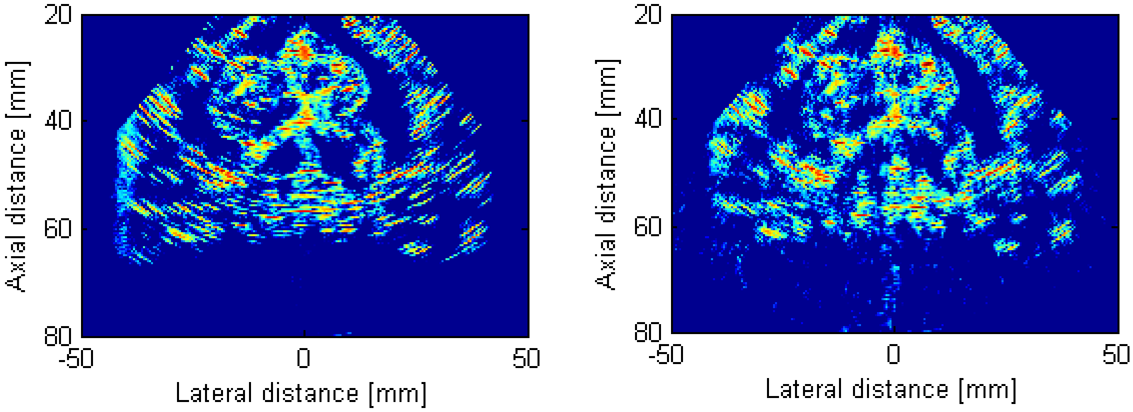

(c) Beamformed Image with decimation factor 6: SSIM = 0.9159, MAE = 7.9154 dB

(d) Beamformed Image with decimation factor 10: SSIM = 0.7310, MAE = 10.2748 dB

Figure 21: Beamformed image reconstructed from decimated data for the fetus phantom simulation: (a) No decimation; (b) Decimation factor of 4; (c) Decimation factor of 6; (d) Decimation factor of 10

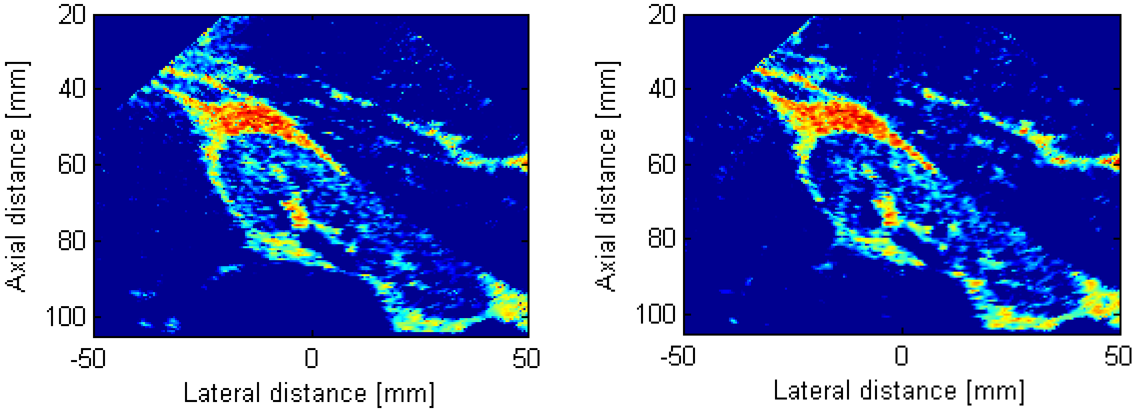

(a) Beamformed Image for Kidney Phantom using original RF data

(b) Beamformed Image with decimation factor 4: SSIM = 0.8796, MAE = 12.8263 dB

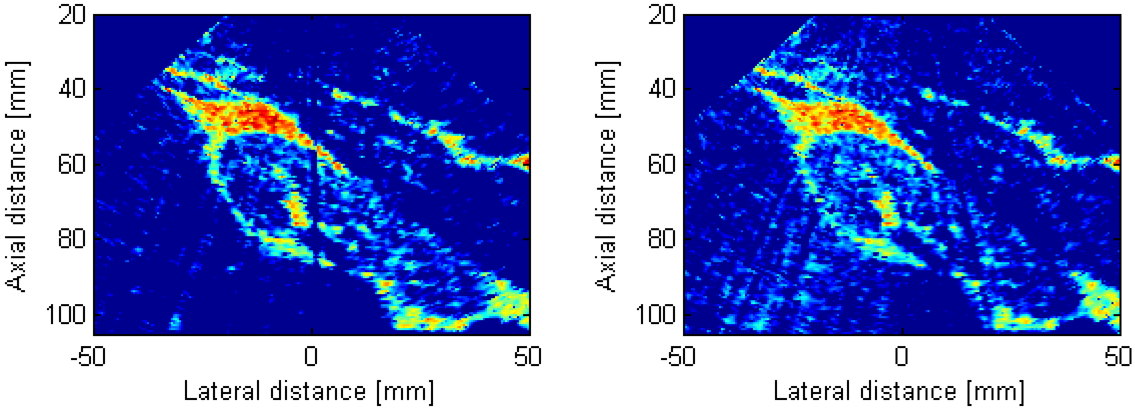

(c) Beamformed Image with decimation factor 6: SSIM = 0.7632, MAE = 14.4527 dB

(d) Beamformed Image with decimation factor 10: SSIM = 0.6795, MAE = 15.3618 dB

Figure 22: Beamformed image reconstructed from decimated data for the kidney phantom simulation: (a) No decimation; (b) Decimation factor of 4; (c) Decimation factor of 6; (d) Decimation factor of 10.

Chapter 4
Introduction to Time Reversal

A necessary condition for compressive sensing (CS), introduced in Chapter 3, is channel sparsity, which is satisfied when the number of scatters relative to the number of available snapshots is small. Natural mechanisms such as ultrasound imaging of a section of a human body include multipath due to secondary reflections. Each multipath introduces its own set of unknown parameters decreasing the sparsity in the backscatter observations. Multipath has a detrimental effect on the performance of the CS based ultrasound imaging mechanism. The principle of time reversal (TR) has been applied to multipath scattering medium, where explicit modeling of the medium is difficult due to random perturbations in the medium. Chapter 4 introduces the principal of time reversal, while Chapter 5 applies TR to the CS mechanism introduced in Chapter 3 to deal with the multipath distortions introduced in scattering environments with rich clutter.

4.1 What is Time Reversal

The principle of TR is applicable to waves described by time-reversal-invariant equations, which contain only derivatives of even orders. TR consists of two steps. First, the backscatter of the channel probing signal is recorded by an array of receiving transducers for duration *T*. The second step time reverses the recorded observations $u(r, t)$, which results in the time reversed signal waveform $u_{TR}(r, t) = u(r, T - t)$. The time-reversed signals are then retransmitted into the medium. The backscatter observations of the time reversed probing signals $u_{TR}(r, t)$ form the time reversal observations used for beamforming.

TR is based on the reciprocity property of wave propagation, which states that the received signal at location r_r reflected from a source located at r_s is identical to the received signal at location r_s originating from a source located at r_r [16]. In other words, the role of the source and observation sites can be reversed.

It has also been shown that the time reversed observations converge at the location of the source (scatter), when transmitted back into the medium. This phenomenon is called "super resolution focusing" with the energy in the recorded observations redistributed in favor of direct reflections from the scatters versus the secondary multipath [17]–[19].

4.2 Time Reversal Implementation Using Field II

In this thesis, TR was implemented physically using Field II by retransmitting the backscatter of the probing signal reflected from the region of interest. TR signals are calculated using two different configurations, namely the single input multiple output (SIMO) and multiple input multiple output (MIMO) configurations. TR using the SIMO setup is applied using two steps. The first step is to collect the backscattered signals from the region of interest at all transducer elements when only one transducer element transmits a probing signal as illustrated in Fig. 23. The second step time reverses the recorded signals and transmits the time-reversed signals again into the region of interest. The backscatters of the time-reversed signals are used by the beamforming algorithms.

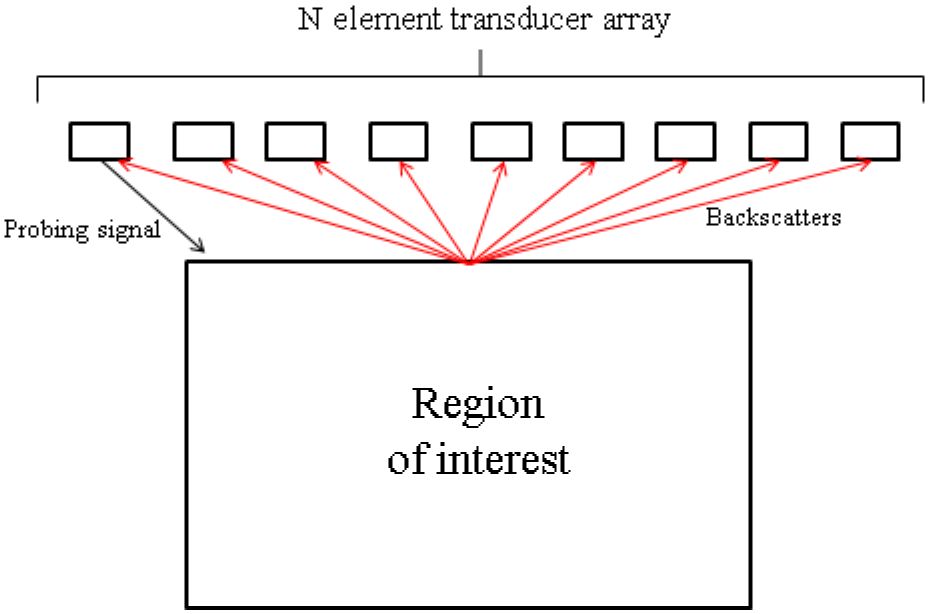

Figure 23: SIMO configuration: Step 1 of the TR mode of operation.

TR using the MIMO configuration is also applied using two steps except that all transmit elements probe the channel in Step 1. The first step is shown in Fig. 24 with all elements transmitting. The backscattered signals reflected from the region of interest are recorded by all transducer elements. The second step is the same as the second step in the TR/SIMO configuration, where the diagonal element signals recorded by the transducers are time reversed and retransmitted again to illuminate the region of interest.

In order to successfully apply TR processing, the probing signals have to be simultaneous and different, they also have to be orthogonal with each other.

After time reversing the signals and retransmitting them into the medium either using the SIMO or MIMO configuration, the backscatters are probed by the compressive sensing system described in Chapter 3. Images reconstructed using the MIMO setup are of much better quality than the ones reconstructed using the SIMO setup as the MIMO backscatters to the transducers array obtained from reflections of the probing signals are much stronger than the SIMO backscatters [20].

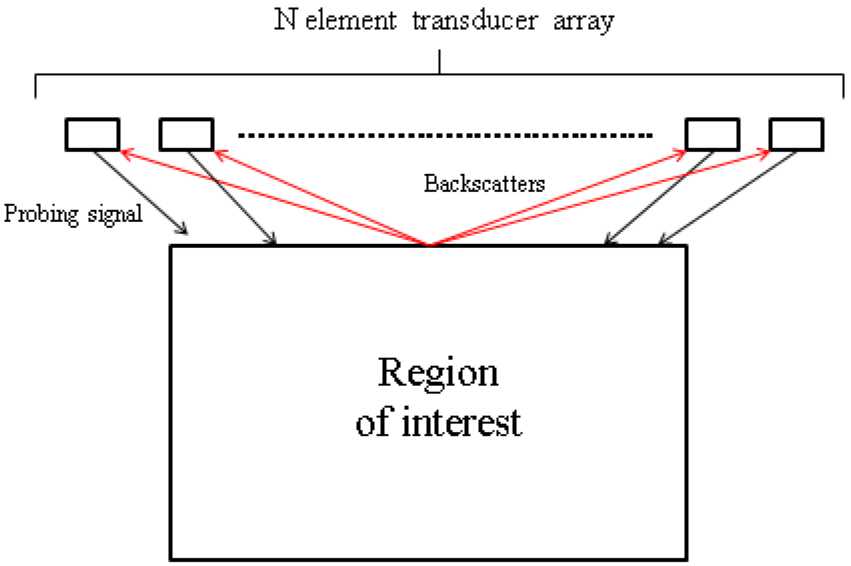

Figure 24: MIMO Configuration: Step of the TR mode of operation.

The complete schematic of the time reversal beamforming system is shown in Fig. 25.

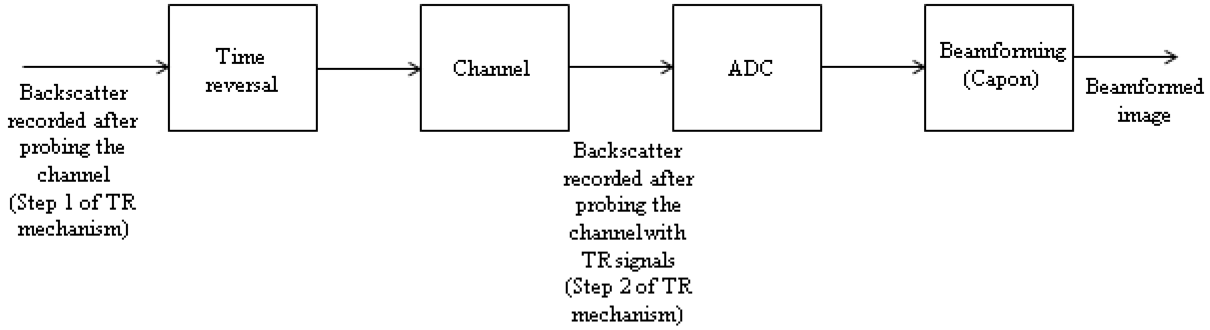

Figure 25: Schematic diagram illustrating how TR is used for beamforming ultrasound system.

4.3 Time Reversal Results

In this section, the Capon beamformed images using signals collected by the two TR configurations are presented for the 5 cyst phantom setup, showing the SSIM and MAE values for a range of SNRs ranging from 20 to 40 dB. For each case, we include the actual reconstructed beamformed images for comparison.

As shown in Figs. 26 and 27, the SSIM values using the MIMO configuration is higher than those obtained from the SIMO setup. The pereceived image quality of the MIMO configuration is also superior to the image quality obtained from the SIMO configuration.

Fig. 28 plots a bar chart comparing the SSIM values for the 5 cyst phantom model using SIMO and MIMO results for reconstructed images with SNRs of 20, 30, and 40 dB. Again, we see significant improvement with the TR/MIMO as compared to the TR/SIMO configuration.

<u>5 cysts phantom results:</u>

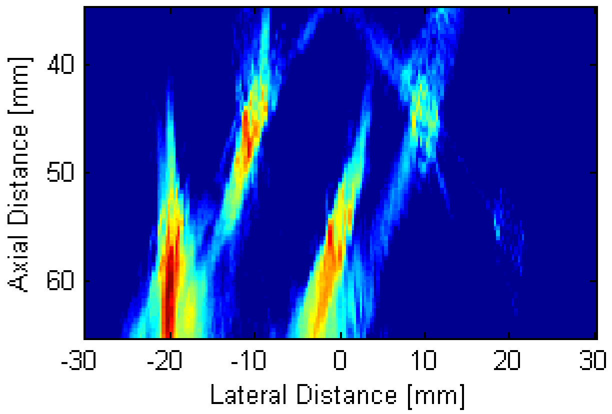

(a) Beamformed image with SNR 20 dB:
SSIM = 0.2043 , MAE = 10.4384 dB

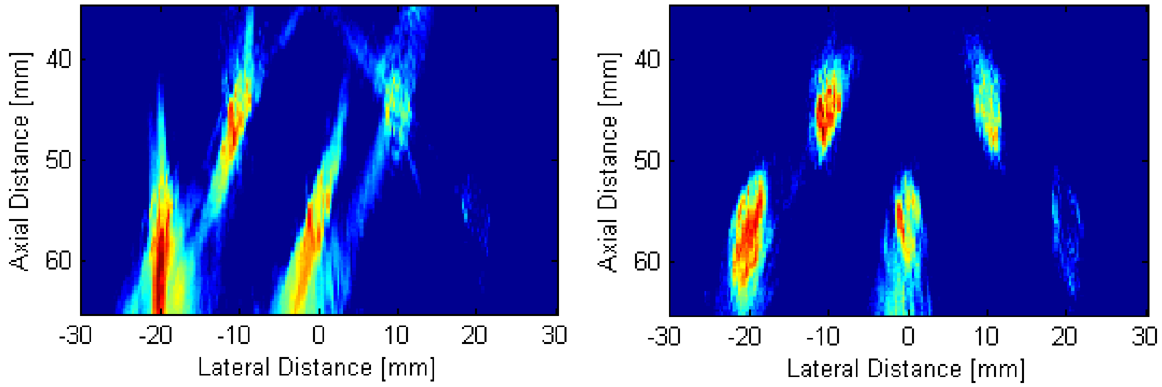

(b) Beamformed image with SNR 30 dB: SSIM = 0.2327, MAE =10.2366 dB

(c) Beamformed image with SNR 40 dB: SSIM = 0.2462, MAE = 9.1792 dB

Figure 26: Beamformed Images for the 5-Cyst phantom setup using the SIMO TR signals for (a) SNR = 20 dB; (b) SNR = 30 dB; (c) SNR = 40 dB.

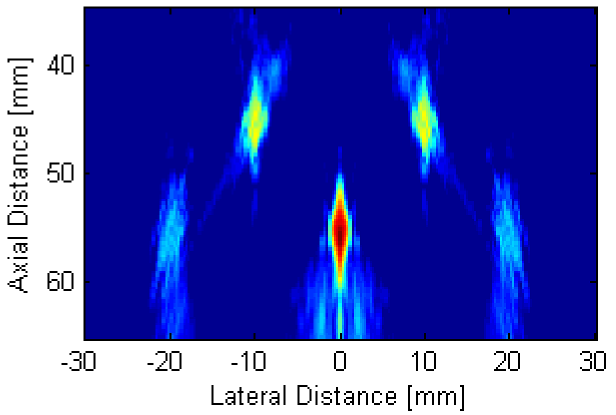

(a) Beamformed image with SNR 20 dB: SSIM = 0.6749 , MAE = 4.9111 dB

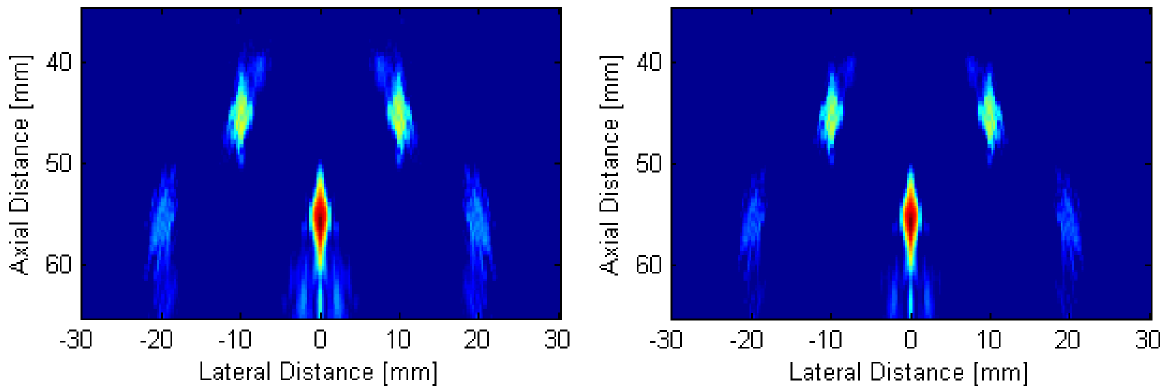

(b) Beamformed image with SNR 30 dB: SSIM = 0.6820 , MAE = 4.8459 dB

(c) Beamformed image with SNR 40 dB: SSIM = 0.6831, MAE = 4.8357 dB

Figure 27: Beamformed Images for the 5-Cyst phantom setup using the MIMO TR signals for (a) SNR = 20 dB; (b) SNR = 30 dB; (c) SNR = 40 dB.

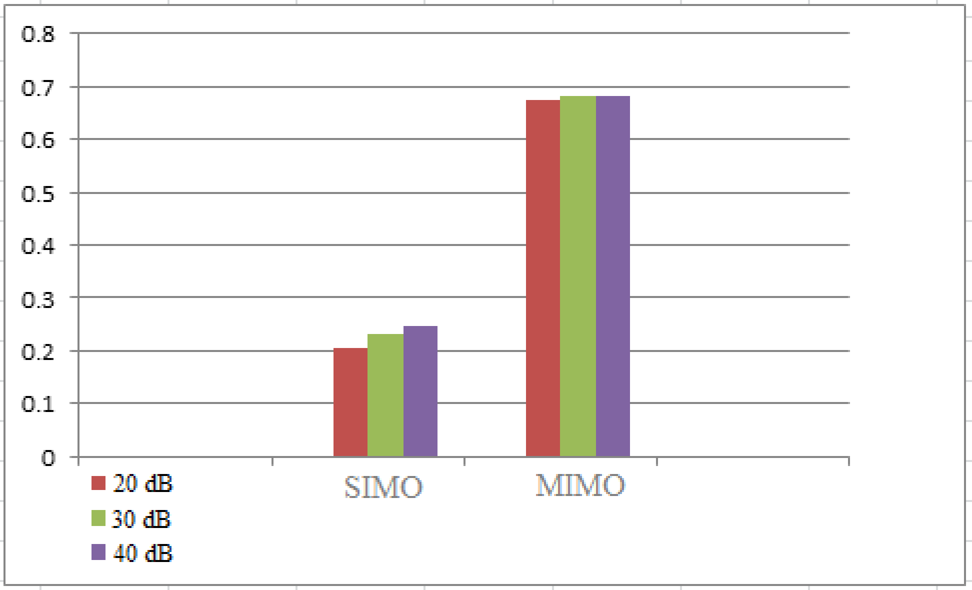

Figure 28: Bar chart comparing SSIM values of MIMO and SIMO configurations for the 5 cyst phantom setup.

Chapter 5
Time Reversal with Compressive Sensing

The ultimate goal and contribution of this thesis is to design a prortable ultrasound machine by decreasing its cost, which can be achieved by acquiring data at low frequencies using Compressive Sensing. This leads to a significant decrease in the sampling frequency of the analog to digital converter. Decreasing the sampling frequencies has a side effect in terms of poor reconstructed image quality due to aliasing. To avoid degraded image quality, the previously explained algorithms (Time Reversal, Compressive Sensing, and Beamforming) are combined. Fig. 29 shows a block diagram for the beamforming mechanism obtained by coupling TR with CS Beamforming.

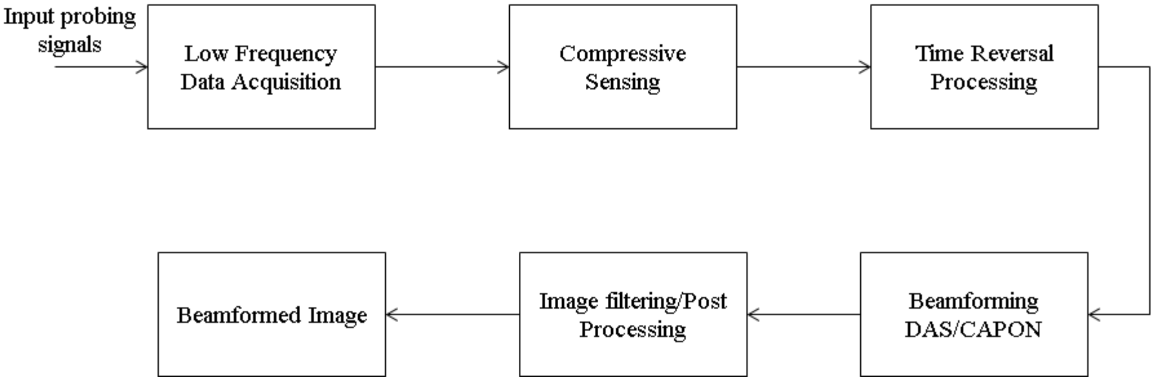

Figure 29: CS TR/BF mechanism that couples time reversal with compressive sensing.

The overall system is referred to as CSTR/BF mechanism.

In Fig. 29, the backscatters received at each transducer element are decimated using different decimation factors to obtain the low frequency data, and then compressive sensing is applied to those backscatters to reconstruct the signals. In order to increase the image quality, the reconstructed signals are time reversed and re-transmitted again into the region of interest using Field II using either the SIMO or MIMO configuration. In each case, we use either the SIMO or MIMO configuration. The backscatters from the time reversed reconstructed signals are processed using the Capon BF algorithm to yield the beamformed reconstruction of the medium.

Another reason for coupling TR with CS/MIMO setup is to reduce the detrimental impact of multipath on the beamformed image. Multipath violates the sparsity condition needed by CS. It is expected that the TR CS/BF algorithm produces better reconstruction than CS BF algorithm alone.

Section 5.1 shows the beamformed images for both the SIMO and MIMO configurations. Images are obtained by applying TR to the signals after reconstructing them at different sampling frequencies for a SNR of 40 dB. The SSIM and MAE values are presented by comparing the reconstructed images of the CS TR/BF mechanism with the image truth for the setup. Section 5.2 compares the images obtained using the CS TR/BF mechanism with the MIMO setup versus the CS BF mechanism alone. This comparison illustrates the superiority of coupling TR with CS.

5.1 Results

5 cyst phantom model results

As shown in Figs. 30, 31 and 32, the SSIM values of the images obtained from the MIMO setup are always higher than the ones obtained using SIMO setup. Similarly, the MAE values obtained from the MIMO setup are always lower than the ones obtained using the SIMO setup. Higher the decimation factor, the lower is the image quality because each signal has to be reconstructed from a reduced number of samples, resulting in lower SSIM values due to increased noise in the reconstructed data.

5.2 Comparison between CS and TR with CS

Having demonstrated the enhancement of the performance with the MIMO setup, we now compare the reconstruction quality of the CS TR/BF setup with CS BF alone. The CS BF reconstruction does not use TR.

Images with decimation factor of 4:

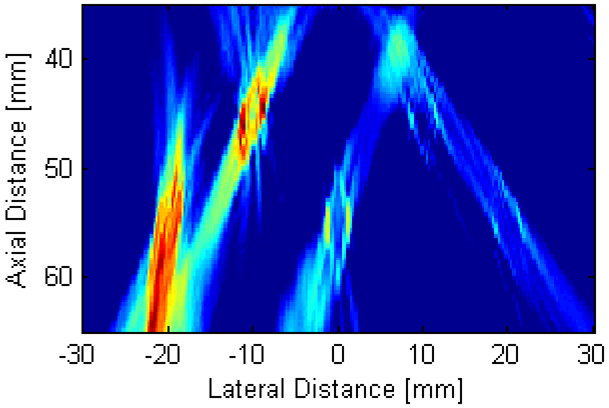

(a) SIMO setup: SSIM = 0.2691,
MAE = 8.9311 dB

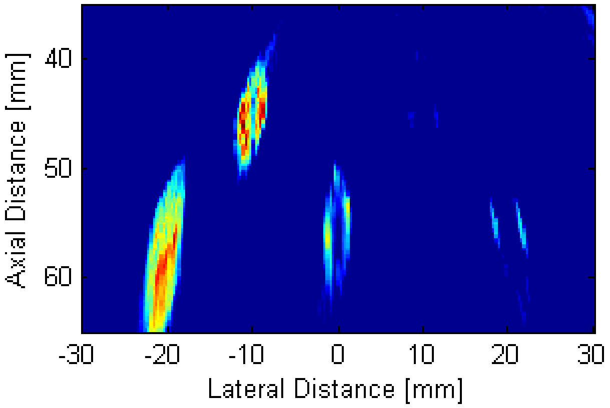

(b) MIMO setup: SSIM = 0.5708,
MAE = 6.3677 dB

Figure 30: Beamformed Images for the 5-Cyst phantom using the CS TR/BF setup, for (a) the SIMO configuration; (b) the MIMO configuration. The decimation factor used in the CS setup is 4.

Images with decimation factor of 6:

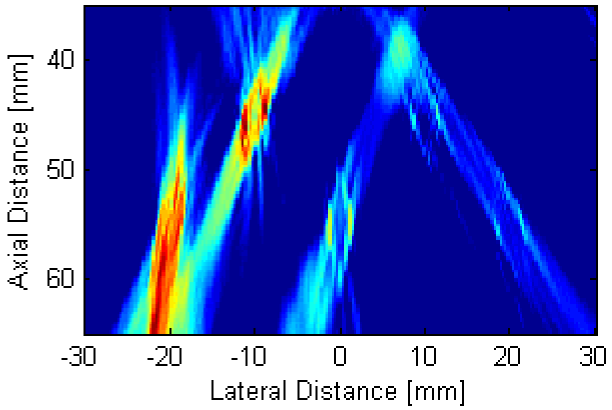

(a) SIMO setup: SSIM = 0.2680, MAE = 7.5568 dB

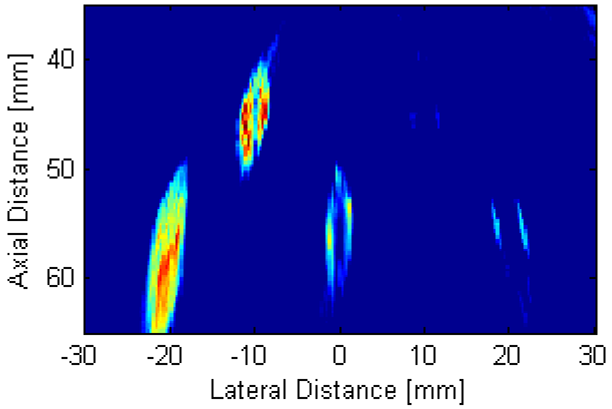

(b) MIMO setup: SSIM = 0.5685, MAE = 6.3844 dB

Figure 31: Beamformed Images for the 5-Cyst phantom using the CS TR/BF setup, for (a) the SIMO configuration, (b) the MIMO configuration. The decimation factor used in the CS setup is 6.

Images with decimation factor of 10:

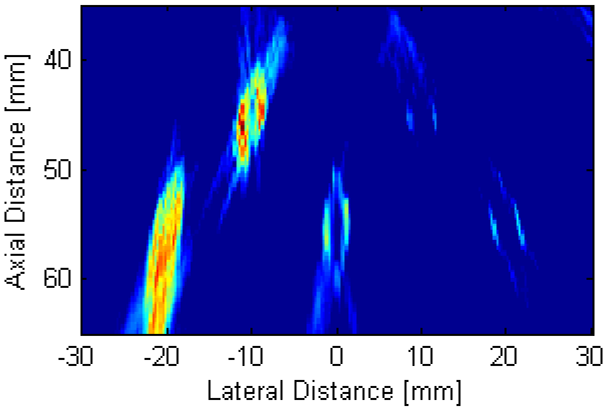

(a) SIMO setup: SSIM = 0.2450, MAE = 8.5345 dB.

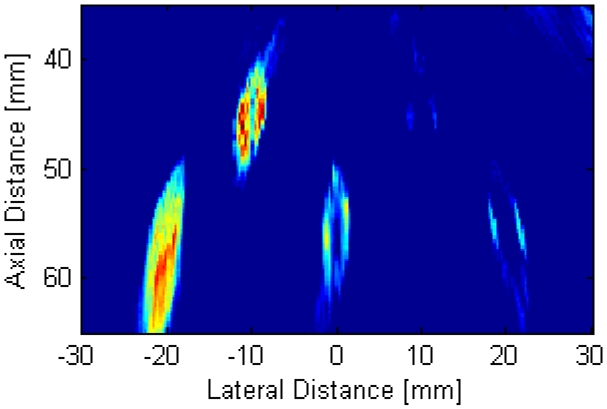

(b) MIMO setup: SSIM = 0.5485, MAE = 7.3844 dB

Figure 32: Beamformed Images for the 5-Cyst phantom using the CS TR/BF setup for: (a) the SIMO configuration; (b) the MIMO configuration. The decimation factor used in the CS setup is 10.

In this section, the SSIM and MAE values of images obtained using signals reconstructed by CS and CS with TR using the MIMO setup are presented for a 5-cyst phantom for a variety of decimation factors. The SSIM values are calculated as follows:

- For the beamformed images obtained using CS only, the SSIM values are calculated between the image truth of the model and the beamformed images obtained after reconstructing the data using CS.
- For the beamformed images obtained using CS with TR, the SSIM values are calculated between the image truth of the model and the beamformed images obtained after applying CS with TR.

Fig. 33 shows that both subjective and objective quality of the beamformed images using signals reconstructed using CS then further processed with TR techniques is much better than the beamformed images using signals reconstructed using CS only without any further processing.

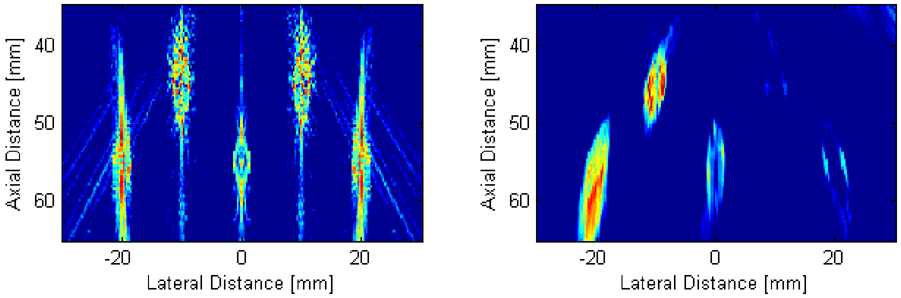

(a) Images with decimation factor of 4:
=[left SSIM = 0.0998, Right SSIM = 0.5708

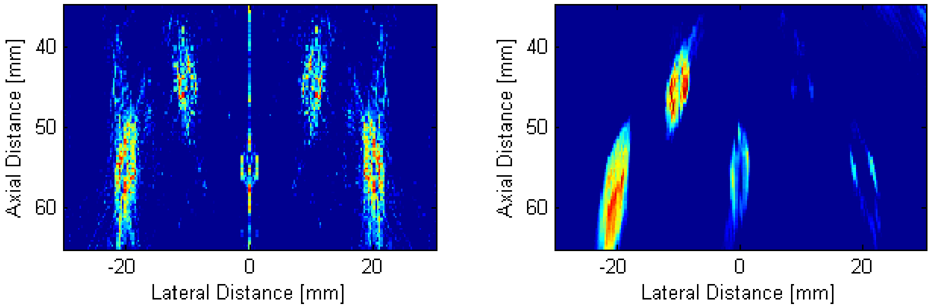

(b) Images with decimation factor of 6:
Left SSIM = 0.0970, Right SSIM = 0.5685

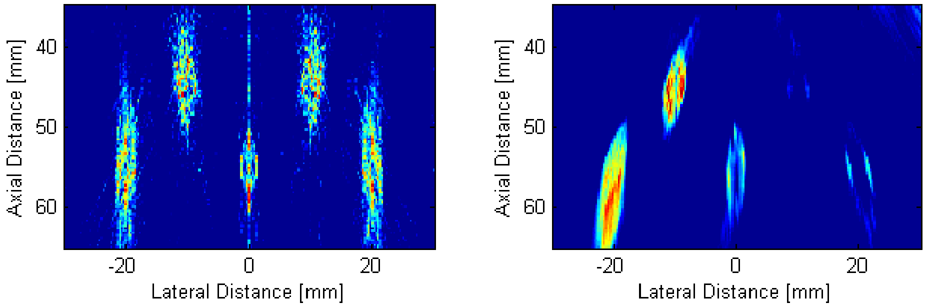

(c) Images with decimation factor of 10:
Left SSIM = 0.0960, Right SSIM = 0.5485

Figure 33: Comparison between images obtained using reconstructed RF data with CS versus reconstructed RF data using CS TR processing for different decimation factors: (a) Decimation factor of 4; (b) Decimation factor of 6; (c) Decimation factor of 10

Summary

The thesis incorporates the TR principle and CS in CAPON beamforming with a linear array using MIMO configuration for ultrasound applications. The proposed CS TR /BF algorithm uses multipath constructively to focus the TR probing signals on to the targets. The CS TR /BF algorithm system outperforms the CS BF system in the Monte Carlo simulations based on Field II for a multicyst setup.

Chapter 6
Conclusions

In this thesis I used Field II, a MATLAB toolbox as a simulation setup to generate ultrasound fields for testing my beamforming algorithms. I focus on two beamforming techniques namely, the DAS algorithm and the Capon algorithm for a variety of setups, including the 2-point and 10-point scatters field, 5-cyst and 10-cyst framework, the kidney phantom, and the fetus phantom within the human body. The results presented for all implemented models illustrate that the Capon algorithm is superior in regards to image reconstruction and localization of the abnormalities like cysts in the human body.

The main goal of this thesis is to acquire data at sampling rates far below the Nyquist rate without introducing the aliasing effect. I implemented the recently proposed compressive sensing (CS) algorithm for data compression and coupled CS with novel data acquisition (sensing) approached and basis representation in order to achieve near-optimal full length signal reconstruction. I tested my algorithms with simple models as point scatters then complicated the model to represent real body parts such as the kidney and fetus phantoms. In each case, images were reconstructed using data with different subsampling frequencies.

Results show that CS reconstruction is successful with subsampling of up to 90%. In other words, the CS data is only 10% of the original data. The quality of the reconstruction was tested through the structural similarity index matrix (SSIM) at various subsampling rates.

In order to increase the quality of the images obtained using reconstructed signals, the time reversal (TR) processing techniques were physically implemented using Field II with two different array setups, namely, the MIMO and SIMO configurations, showing that MIMO setup is superior to the SIMO setup. The resulting TR CS/BF framework is suitable for complex environments such as ultrasound applications on human body that have rich multipath due to clutter noise.

Images using the TR CS/BF framework with MIMO configuration were presented for different signal sampling frequencies at a SNR of about 40dB. Results show that with a CS subsampling rate of 90%, the SSIM value between the image obtained by CS with TR and the model image truth improved by a factor of 5.7 as compared to the SSIM of the image derived using reconstructed signals based on the CS only. In each case, the model image truth was used for reference.

Future Work

There are two main directions in which my research in the TR CS/BF framework can be extended. First, applying the beamforming framework to reconstruct the representation of complex environments such as the human kidney and fetus phantoms is proposed. The second direction is to construct an experimental setup based on the Field II simulation environment where the proposed algorithms can be applied with real signals and phantom representations of the human body.

The research presented in this thesis is very much based on simulations. More theoretical analysis need to be done to confirm the superiority of the TR CS/BF framework over the CS/BF framework without time reversal. Such an analysis can, for example, include the Cramer Rao performance bounds for the two setups. Finally, the compressibility aspects of CS in the TR CS/BF framework can be analyzed to see the extent of compressibility possible in the RF data.

Bibliography

[1] J. A. Jensen, “Field: A Program for Simulating Ultrasound Systems,” medical and Biological Engineering and Computing, vol. 34. Pp. 351-353, 1996.

[2] J. Capon, “High-resolution frequency-wavenumber spectrum analysis,” *Proc. IEEE*, vol. 57, pp. 1408–1418, Aug. 1969.

[3] J. A. Mann and W. F. Walker, “A constrained adaptive beamformer for medical ultrasound: Initial results,” Proc. IEEE Ultrason. Symp., vol. 2, pp. 1807–1810, Oct. 2002.

[4] Magali Sasso and Claude Cohen-Bacrie, “Medical ultrasound imaging using the fully adaptive beamformer,” Proc. IEEE Int. Conf. Acoust. Speech, Sign. Proc., vol. 2, pp. 489–492, March 2005.

[5] Zhisong Wang, Jian Li, and RenbiaoWu, “Time-delay- and time reversal-based robust Capon beamformers for ultrasound imaging,” IEEE Trans. Med. Imag., vol. 24, pp. 1308–1322, Oct. 2005.

[6] K. Holfort, F. Gran, and J. A. Jensen, “Minimum variance beamforming for high frame-rate ultrasound imaging,” Proc. IEEE Ultrasonics Symposium, pp.1541–1544, Oct. 2007.

[7] S. Holm, J.-F Synnevåg, A. Austeng, “Capon Beamforming for Active Ultrasound Imaging Systems,” Digital Signal Processing Workshop and IEEE 13th DSP Workshop, Jan. 2009.

[8] J.-F Synnevåg, A. Austeng, S. Holm, “Adaptive Beamforming Applied to Medical ultrasound Imaging,” IEEE Transacions on Ultrasonics,

Ferrorlrctrics and Frequency Control, vol. 54, no. 8, pp. 1606-1613, Aug 2007.

[9] Zhou Wang, Alan C. Bovik,Hamid R. Sheikh, Eero P. Simoncelli, “Image Quality Assessment: From error Visibility to Structutal Similarity,” IEEE Transactions on Image Processing, vol. 13, pp. 600-012, Apr 2004.

[10] Hervé Liebgott, Rémy Prost, Denis Friboulet, “Pre-beamformed RF signal reconstruction in medical ultrasound using compressive sensing,” IEEE Ultrasonics Symposium, 2010.

[11] D. Friboulet, H. Liebgott, R. Prost, “Compressive sensing for raw RF signals reconstruction in ultrasound,” IEEE Ultrasonics Symposium, San Diego, California, USA, Oct 2010.

[12] Laurent Demanet, Lexing Ying “Wave Atoms and Sparsity of Oscillatory Patterns,”Ph.D. dissertation, Math Dept. Stanford Univ., Stanford and Texas Univ., Austin, 2006.

[13] Abdul A. Mohammed, Rashid Minhas, Q.M. Jonathan Wu, Maher A. Sid-Ahmed, “Fingerprint Image Compression Standard Based on Wave Atoms Decomposition and Self Organizing Feature Map,” IEEE International Conference on Image Processing, pp. 2837-2840, 2009.

[14] L. Demanet, Curvelets, Wave Atoms and Wave Equations, Ph. D. thesis, California Institute of Technology, 2006.

[15] Gesen Zhang, Shuhong Jiao, Xiaoli Xu, Lan Wang, “Compressive Sensing and Reconstruction with Bernoulli Matrices,” IEEE International conference on Information and Automation, pp. 455-460, 2010.

[16] P. M. Morse and K. U. Ingard. Theoretical Acoustics. McGraw-Hill, New York, 1st edition, 1968.

[17] P. Blomgren, G. Papanicolaou, and H. Zhao, "Super-resolution in time-reversal acoustics," Journal of the Acoustical Society of America, 111, 230-48, 2001.

[18] C. Tsogka and G. C. Papanicolaou, "Time reversal through a solid-liquid interface and super-resolution," Inverse problems, vol. 18, no. 6, pp. 1639–1657, 2002.

[19] M. Fink, "Time reversal of ultrasonic fields- Part I: Basic principles," IEEE Transactions on Ultrasonics, Ferroelectrics and Frequency Control, vol. 39, no. 5, pp. 555–566, Sep. 1992.

[20] Y. Jin, J. Moura, and N. O'Donoughue, "Time reversal in multiple-input multiple-output radar," *Selected Topics in Signal Processing, IEEE Journal of*, vol. 4, pp. 210 –225, Feb. 2010.

[21] Emmanuel J. Candes and Micheal B. Wakin, "An Introduction to Compressive Sampling,"IEEE Signal Processing Magazine, March 2008.

[22] Hongteng Xu and Guangtao Zhai, "ECG data compression based on Waveatom transform, "IEEE 13th Workshop on MultiMidea Signal Processing (MMSP), pp.1-5, Oct. 2011

[23] Laurent Demanet, "Curvelets, Waveatoms and Wave Equations, " PhD. Dissertation, California institute of technology, Pasadena, California, USA, May 2006.

[24] F. Foroozan and A. Asif, Time reversal based active array source localization, IEEE Transactions on Signal Processing, vol. 59, no. 6, pp. 2655-2668, Jun. 2011.

[25] F. Foroozan and A. Asif, Cramer-Rao bound for time reversal active array direction of arrival estimators in multipath environments, IEEE

International Conference on Acoustics, Speech, and Signal Processing (ICASSP), pp. 2646-2649, Mar. 2010.

[26] F. Foroozan, A. Asif, Y. Jin, and J. Moura, Direction finding algorithms for time reversal MIMO radars, IEEE Statistical Signal Processing Workshop (SSP), pp. 433-437, 2011.

[27] F. Foroozan and A. Asif, Time reversal MIMO radars for estimation of velocity and direction, IEEE Statistical Signal Processing Workshop (SSP), pp. 860-863, 2012.

[28] F. Foroozan, A.Asif, and R. Boyer, Angular Resolution Limit for The Time Reversal MIMO Radar, IEEE International Conference on Acoustics, Speech, and Signal Processing (ICASSP), pp. 4125-4129, 2013.

[29] M. Sajjadieh and A. Asif, Uniform rectangular time reversal arrays: Joint azimuth and elevation estimation, IEEE Statistical Signal Processing Workshop (SSP), pp. 89-92, 2012.

[30] M. Sajjadieh and A. Asif, Compressive Sensing Time Reversal MIMO Radar: Joint Direction and Doppler Frequency Estimation, IEEE Signal Processing Letters , vol. 22, no. 9, pp. 1283-1287, Feb. 2015.

[31] F. Foroozan, A. Asif and Y. Jin, Cramer-Rao Bound Improvement in Angle-Velocity Estimation with the Time Reversal MIMO Radar, submitted to IEEE Transactions on Aerospace and Electronic Systems, 2015. Manuscript of 30 pages.

[32] M. Sajjadieh and A. Asif, Joint Time Reversal and Compressive Sensing based Localization Algorithms for Multiple-Input Multiple-Output Radars, in Proceedings of IEEE International Conference on Acoustics, Speech, and Signal Processing (ICASSP), pp. 2354-2359, 2015.